Engineering Structures 311 (2024) 118189

Contents lists available at ScienceDirect

Engineering Structures

journal homepage: www.elsevier.com/locate/engstruct

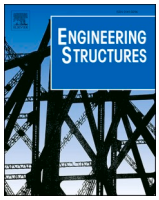

Quantifying the seismic performance factors of half-elliptic-braced steel moment frames (HEB-MFs)

Alireza Shirpour, Nader Fanaie *

Department of Civil Engineering, K. N. Toosi University of Technology, Tehran, Iran

ARTICLE INFO

Keywords:
Half-elliptic-braced steel moment frames (HEB-MFs)
Unbalanced vertical force
Seismic performance factors (SPFs)
FEMA P695 procedure
Incremental dynamic analysis (IDA)

ABSTRACT

Chevron or inverted V-braced frames (IVBFs), despite their high stiffness and strength, exhibit weak post-buckling behavior. In these systems, the buckling of the brace's compressive member in a particular story causes an unbalanced vertical force at the mid-span of the beam, leading to the concentration of damage in that story and, ultimately, the collapse of the structure. This paper aims to propose and investigate a novel bracing system called the half-elliptic-braced steel moment frame (HEB-MF) to overcome the drawbacks of conventional IVBFs. This system is composed of two quarter-elliptic bracing members. The elliptical geometry of these bracing members not only mitigates the unbalanced force and deflection at the beam's mid-span but also enhances energy absorption. At the outset, the hysteric performance of this bracing system is evaluated in comparison with the IVBF system. Afterward, considering eight three-dimensional archetypes with varying numbers of stories in two distinct seismic design categories (SDC C_{max} and C_{min}), the seismic performance factors (SPFs) of this system are determined based on the FEMA P695 procedure, and the fragility curve is plotted for each archetype. The results reveal that employing this system not only effectively reduces the unbalanced force and beam deflection but also enhances ductility and energy absorption compared to the IVBF systems. Furthermore, this system's response modification, over-strength, and deflection amplification factors have been obtained as 7.5, 3, and 7.5, respectively.

1. Introduction

Concentrically braced frames (CBFs) outperform other structural systems in effectively reducing lateral displacements in steel structures when confronted with lateral forces. The chevron-braced frame is one of the configurations of CBFs and possesses dynamic stability characteristics, especially during strong earthquakes. Due to lateral displacements caused by an earthquake, the compressive member of this bracing system undergoes dynamic buckling, resulting in a gradual reduction in its axial strength. Meanwhile, the force on the tensile member can increase until it reaches the yield point. The consequence of this process will be the emergence of an unbalanced vertical force in the mid-span of the beam. The formation and expansion of non-linear behavior characteristics with large amplitude in the beam element and the support connections exacerbate the probability of soft-story mechanism formation. In order to reduce the occurrence probability of the described circumstance, which is accompanied by dynamic instability, it is necessary to design a stronger beam. It is obvious that the disproportionate observance of this criterion will lead to the design of a resistant but uneconomical structure [1–7]. Several approaches have been proposed in recent years to overcome the unbalanced vertical force and beam deflection in chevron-braced frames. Among them, certain approaches counteract the unbalanced vertical forces by using zipper columns [8–10] and employing a strong beam in the braced spans [11,12]. Additionally, some approaches aim to prevent the emergence of unbalanced forces in the beam of the braced span. These methods include using buckling restrained braces (BRBs) [13,14], employing V-shaped braces and inverted V-shaped braces simultaneously (split-X braces) [15–17], and utilizing a reduced brace section (RBS) or a brace with different geometry [18,19]. Implementing localized structural fuses within specific segments of the bracing members' length is one of the methods that can not only resolve the problem of unbalanced vertical forces but also enhance the ductility and energy absorption of CBFs [20,21]. Rezai et al. examined the cyclic load-displacement hysteretic curves of CBFs by implementing elliptical-shaped incisions as structural fuses in HSS bracing members [22]. Bontetti evaluated the performance of CBFs by incorporating an oval cut at the termination of the bracing member [23]. Ahlehagh and Mirghaderi proposed balanced bracing systems to

* Correspondence to: K. N. Toosi University of Technology, Civil Engineering Department, No. 1346, Vali-Asr Street. P.O. Box. 15875-4416, 19697 Tehran, Iran.
E-mail address: fanaie@kntu.ac.ir (N. Fanaie).

https://doi.org/10.1016/j.engstruct.2024.118189
Received 30 August 2023; Received in revised form 28 April 2024; Accepted 10 May 2024

enhance the behavior of inverted V-braced frames (IVBFs), counteracting the unbalanced force and reducing the discrepancy between tensile and compressive capacity values. In these bracing systems, the tensile or compressive yielding capacity decreases by reducing the cross-sectional area of a portion of the bracing member's length. However, with the consideration of appropriate details, the buckling capacity of the bracing system does not undergo a significant change [19]. In order to improve seismic performance and reduce seismic demand in the connections of angle-shaped CBF, Legeron et al. conducted a comprehensive investigation on ductile fuses. In this empirical study, they established a ductile fuse at a defined distance from both ends of the angle-shaped bracing members, designed with a tensile capacity lower than that of the bracing connection [24]. Kachooee and Kafi focused on enhancing the behavior of CBFs by introducing a novel approach, utilizing both experimental and numerical studies. They utilized a localized fuse along the length of the bracing member, enclosing it with auxiliary elements to prevent localized buckling under compressive loading [18]. Over the past two decades, researchers have utilized ductile bending elements as fuses in bracing systems due to their increased deformation amplitude, introducing novel perspectives. In this regard, notable research has been carried out by Bazzaz et al. and Andalib et al., focusing on the application of steel rings to enhance ductility and augment energy absorption in bracing systems. The load-carrying capacity of the steel ring in these bracing systems is a function of its length, radius, thickness, and yield stress. This enables the possibility of designing a ring element proportional to the structural requirements by altering any of these factors [25–28]. Trombetti et al. developed crescent-shaped brace (CSB) systems to eliminate the buckling issue of CBFs in the performance-based seismic design framework. They found that employing this bracing system in buildings mitigates the risk of creating the first soft-story and overall building instability owing to hardening at large deformations caused by geometric non-linearity as well as symmetric cyclic behavior [29]. Through comprehensive analytical and experimental studies on CSBs, Palermo et al. discovered that these bracing systems possess notable ductility capacity and ultimate hardening, efficiently averting damage from second-order effects. Furthermore, their research findings indicated that the initial yield strength and initial lateral stiffness in these braces are independent, and they can serve as a viable alternative to BRBs due to their sustainable cyclic behavior and energy dissipation without stiffness and strength deterioration [30–33]. Omar et al. also assessed the performance of CSBs by utilizing pushover and time history analyses. They examined their applicability to multi-story concrete structures with shear behavior [34]. In order to reduce the drawbacks of CBFs and enhance their ductility and energy absorption capacity, Jouneghani et al. proposed elliptical braced systems, while Boostani et al. suggested circular (OGrid) braced system [35–39]. Moreover, Jouneghani et al. presented a precise approach for determining elliptical braced systems' elastic lateral stiffness, employing strain energy and Castigliano's theorem [40,41]. One notable disadvantage of these two bracing systems is the connection between bracing members and columns, as improper implementation and the imposition of high shear forces from these members to the columns elevate the possibility of creating a plastic hinge at the middle of the column [42–44]. Shamivand and Akbari resolved the issue of these two bracing systems using quasi-columns and introduced novel ring-shaped braces called Shami lateral bracing (SLB) systems [45]. Fanaie and Shirpour proposed a solution to the problems of earlier CBF systems and the absence of connection between bracing members and frame members (columns and beams) by introducing a new bracing system termed the quarter-elliptic-braced steel moment frame (QEB-MF). In addition to presenting a precise analytical formulation for computing the elastic stiffness of these systems employing Castigliano's theorem and concepts of strain energy, they assessed their seismic performance under near-field and far-field ground motion records compared with moment-resisting frames [46,47]. In continuing their investigation, they introduced two innovative quasi-x bracing systems with quarter-elliptic members and thoroughly evaluated the performance of moment-resisting frames equipped with these braces using analytical and numerical methods [48,49].

In order to effectively employ and design a lateral force-resisting system as a conventional structural system while adhering to the regulations outlined in the codes, it is imperative to ascertain its seismic performance factors (SPFs), including the response modification factor (R), deflection amplification factor (C_d), and over-strength factor (Ω). The R factor is utilized in seismic loading standards to attenuate the forces imposed on structures due to their non-linear behavior and ductility. When structures are designed for reduced forces, the resulting displacement values are lower than the actual displacements of the structures during earthquakes. Hence, the C_d factor is utilized in seismic codes to predict actual structural displacements. In the design of a ductile structure, the behavior of certain members may be brittle. Therefore, to tackle this issue and in accordance with seismic standards, they are designed for a greater force employing the Ω factor [50,51]. The response modification factor (R) was initially presented in the ATC3–06 report, which was based on observations of previous earthquakes [52]. Afterward, this factor underwent refinement in the ATC-19 and ATC-34 reports [53,54]. Numerous researchers have endeavored to determine the R factor for various bracing configurations using the provided methods. Maheri and Akbari investigated the R factor of X and knee braces [55]; Kim and Choi examined the R factor of chevron braces [56]; and Mahmoudi and Zaree scrutinized the R factor of X, V, and inverted V braces [57].

Recently, new approaches have been suggested for estimating the R factor based on the base shear obtained from incremental dynamic analysis (IDA). Notably, the Mwafy and Elnashai approach stands out in this regard [58]. By employing this method, Fanaie and Ezzatshoar determined the R factor of gate braces [59], and Jouneghani et al. obtained the R factor of elliptical braces [43]. The emergence of modern structural systems necessitated the development of a comprehensive and reliable method for assigning values to SPFs. The FEMA P695 procedure, which is based on probabilistic analyses and the fragility curves resulting from the earthquake spectrum, provided a comprehensive methodology for determining these factors [60]. Utilizing this methodology, Farahi and Mofid quantified SPFs for chevron knee bracing systems [61]; Asghari and Saharkhizan for knee-element connections frames (KCFs) [62]; Ghasemi et al. for cable-cylinder bracing systems [63]; Shahiditabar et al. for self-centered y-shaped (SCY) bracing systems [64]; and Bakhshivand et al. for special moment frames combined with special concentrically braced frames (SMF-SCBFs) [65].

This study investigates the novel half-elliptic-braced steel moment frame (HEB-MF) system. The elliptical geometry of this bracing system effectively reduces unbalanced force and beam deflection, which is a key challenge in chevron or inverted V-braced frames (IVBFs). This bracing system is initially modeled using Abaqus software and subjected to cyclic loading. This system's hysteresis curves, energy dissipation, unbalanced force, and beam mid-span deflection are assessed compared to the IVBF system. Then, the seismic performance factors (SPFs) of HEB-MFs are quantified as per the FEMA P695 procedure. To accomplish this, eight three-dimensional archetypes with varying numbers of stories are designed in two separate seismic design categories (SDC C_{max} and C_{min}) based on presumed SPFs. Utilizing OpenSees software, non-linear models of each archetype are constructed. The period-based ductility (μ_T) and the over-strength factor (Ω) are specified through non-linear static (pushover) analysis. In addition, incremental dynamic analysis (IDA) is carried out utilizing 44 far-field ground motion (FFGM) records to evaluate structural collapse capacity and compute the adjusted collapse margin ratio (ACMR). The accuracy of the initial R factor is assessed by comparing the acquired ACMRs from IDA curves with the acceptable values provided in FEMA P695. Finally, the deflection amplification factor (C_d) and over-strength factor (Ω) for HEB-MFs are determined according to FEMA P695.

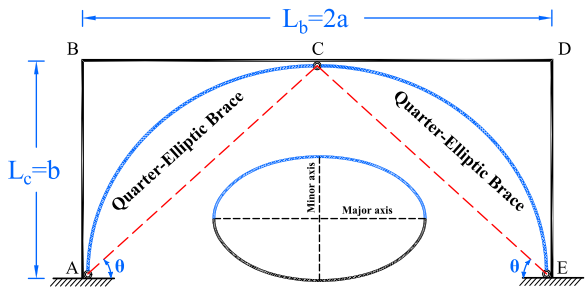

Fig. 1. Geometry of HEB-MF systems.

2. Design procedure for the quarter-elliptic bracing members

The HEB-MF systems are comprised of two quarter-elliptic bracing members. According to Fig. 1, these members have been designed so that the semi-major axis (a) of the ellipse equals the half-beam length ($L_b/2$), and the semi-minor axis (b) of the ellipse equals the column length (L_c).

If this system is subjected to lateral load, an axial force P_b is applied to both sides of the quarter-elliptic bracing member *CE*. As illustrated in Fig. 2a, when the bracing member *CE* encounters the axial force P_b, an additional moment ($P_b e$) is established owing to its eccentricity. To determine the eccentricity length, it is required to initially draw the diameter that connects the endpoint of the semi-major axis (vertex) to the endpoint of the semi-minor axis (co-vertex) in the first quarter of an ellipse, as depicted in Fig. 2b. The diameter *CE* equation is as follows:

$$y = -\frac{b}{a}x + b \tag{1}$$

Subsequently, it is necessary to draw a tangent parallel to the diameter *CE* within the first quarter of the ellipse. The tangent *GH* equation is as follows:

$$y = -\frac{b}{a}x + \sqrt{2}b \tag{2}$$

The eccentricity length is equal to the distance between the diameter *CE* and the tangent *GH*, as obtained by Eq. (3):

$$e = \frac{\sqrt{2}b - b}{\sqrt{\left(\frac{b}{a}\right)^2 + 1}} = \frac{\left(\sqrt{2}-1\right)L_b L_c}{\sqrt{{L_b}^2 + 4{L_c}^2}} \tag{3}$$

Conforming to Fig. 2a, the maximum stress (σ_{max}) experienced by the member *CE* subjected to axial force P_b is situated at its internal face and can be calculated through Eq. (4):

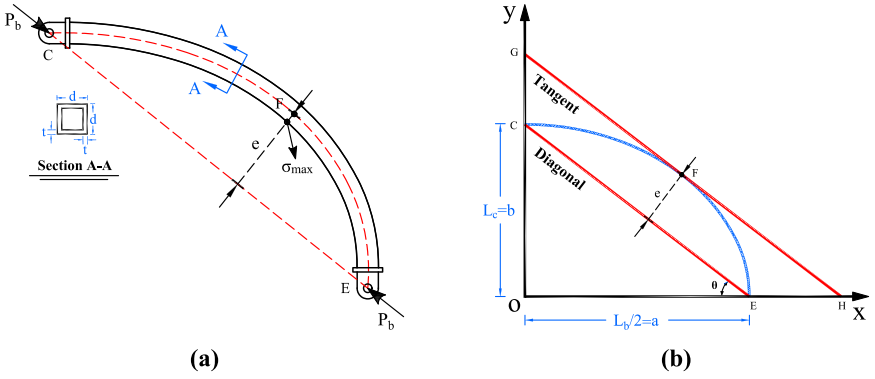

Fig. 2. Quarter-elliptic bracing member *CE*; (a) maximum stress point, (b) coordinate geometry.

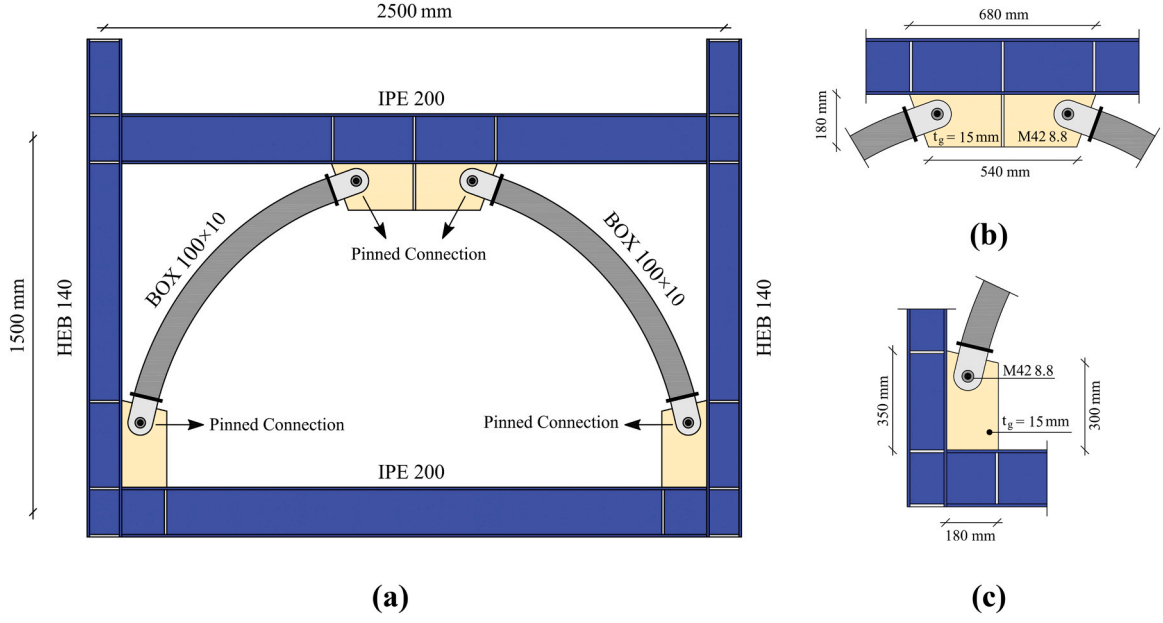

Fig. 3. Half-Elliptic-Braced Steel Moment Frames (HEB-MFs); (a) elevation view, (b) mid-span gusset plate, (c) corner gusset plate.

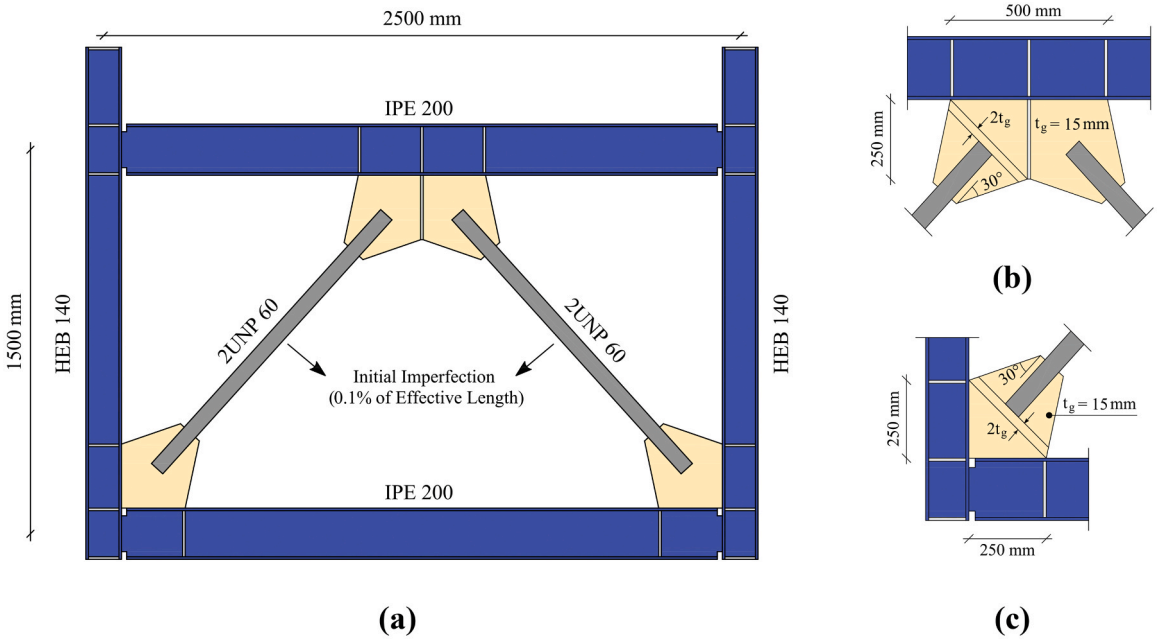

Fig. 4. Inverted V-braced frames (IVBFs); (a) elevation view, (b) mid-span gusset plate, (c) corner gusset plate.

Table 1
Geometric properties of the members in the studied frames.

Members	Section	Depth (mm)	Width (mm)	Web thickness (mm)	Flange thickness (mm)
Column	HEB 140	140	140	7	12
Beam	IPE 200	200	100	5.6	8.5
Half-elliptic brace	BOX 100 × 10	100	100	10	10
Inverted-V brace	2UNP 60	60	60	6	6

$$\sigma_{\max} = \frac{P_b e\left(\frac{d}{2}\right)}{I_q} + \frac{P_b}{A_q} = \frac{6P_b de}{d^4 - (d-2t)^4} + \frac{P_b}{d^2 - (d-2t)^2} \tag{4}$$

where I_q, d, and t represent the quarter-elliptic bracing cross-section's moment of inertia, depth, and thickness, respectively. When the maximum stress is equivalent to the material yielding stress (σ_y), the bracing member achieves yielding and efficiently dissipates energy. Consequently, yielding strength (P_y) of quarter-elliptic bracing membercan be computed utilizing Eq. (5):

$$P_y = \frac{4t\sigma_y(d^3 - 3d^2t + 4dt^2 - 2t^3)}{d^2 - 2dt + 2t^2 + 3de} \tag{5}$$

In line with this equation, the yielding strength of a quarter-elliptic bracing member relies not only on almost constant parameters such as cross-sectional dimensions and material yielding stress, but also on the bracing member's magnitude of eccentricity. The eccentricity decreases under tensile loading, particularly post-yielding of the bracing member, and is expected to lead to increased stiffness. In contrast, under compressive loading, the eccentricity increases, resulting in decreased stiffness after the bracing member yields.

3. Comparing HEB-MF and IVBF bracing systems

In this section, both the HEB-MF and IVBF bracing systems were modeled using Abaqus finite element software and subjected to identical displacement-controlled cyclic loading to compare their hysteresis curves, energy dissipation, unbalanced force, and mid-span deflection of beams.

3.1. Details of the examined models

The studied HEB-MF and IVBF bracing frames are illustrated in Figs. 3 and 4, respectively. As shown in Figs. 3a and 4a, both frames have a span width of 2.5 *m* and a story height of 1.5 *m*. Furthermore, HEB 140 cross-sections were employed for columns and IPE 200 cross-sections for beams. In the HEB-MF model, BOX 100 × 10 cross-sections were used for braces, while in the IVBF model, 2UNP 60 cross-sections were utilized. The geometric properties of the considered cross-sections are listed in Table 1. In the HEB-MF model, as shown in Fig. 3b and c, beams were connected to columns using rigid connections, and bracing members were linked to the gusset plate through pin connections. In the IVBF model, as illustrated in Fig. 4b and c, all the members are connected through hinge connections, and to accurately simulate the beam-column hinge connections, 80% of the beam web was continued and linked to the column flange.

In addition, the IVBF model's gusset plates were designed using the concept of Whitmore's effective width and considering a linear clearance of $2t_g$ (where t_g is the gusset plate's thickness) [66]. The tie constraint was utilized to model welded connections between steel elements in the Abaqus software. Likewise, for pinned connections, the MPC pin constraint was employed. The S4R element was chosen for the modeling of both frames. This element is a linear four-node element, with each node possessing six degrees of freedom for displacement and rotation, and it utilizes the reduced integration method for solving integrals [67]. Due to the out-of-plane buckling of IVBF bracing members, 0.1% of their effective length based on buckling modes was regarded as an initial geometric imperfection [68]. All components of the two frames were fabricated from S235JR steel grade as per the EN1993–1-1 standard, with $F_y = 235\ MPa$, $F_u = 360\ MPa$ and $E = 210\ GPa$ [69]. The combined hardening model was selected to accurately simulate steel

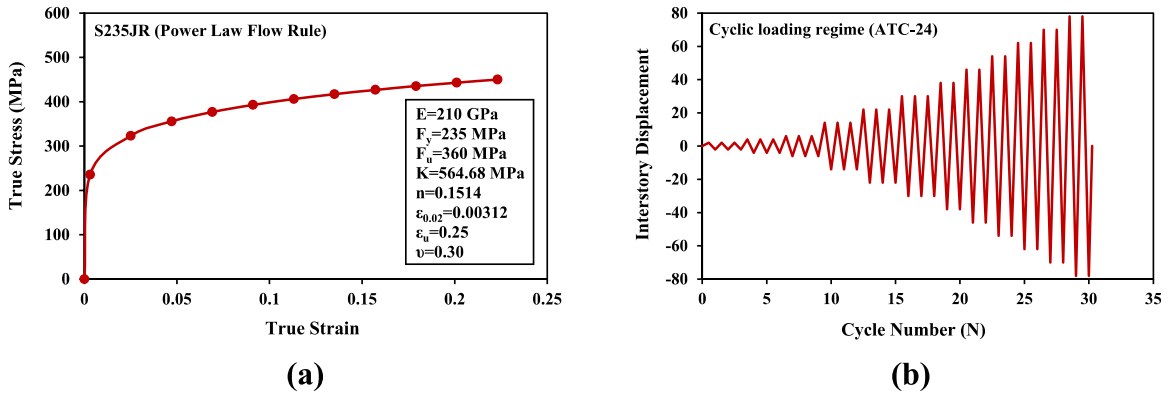

Fig. 5. Abaqus software input data; (a) S235JR steel's true stress-true strain curve, (b) displacement-controlled cyclic loading based on ATC-24 [71].

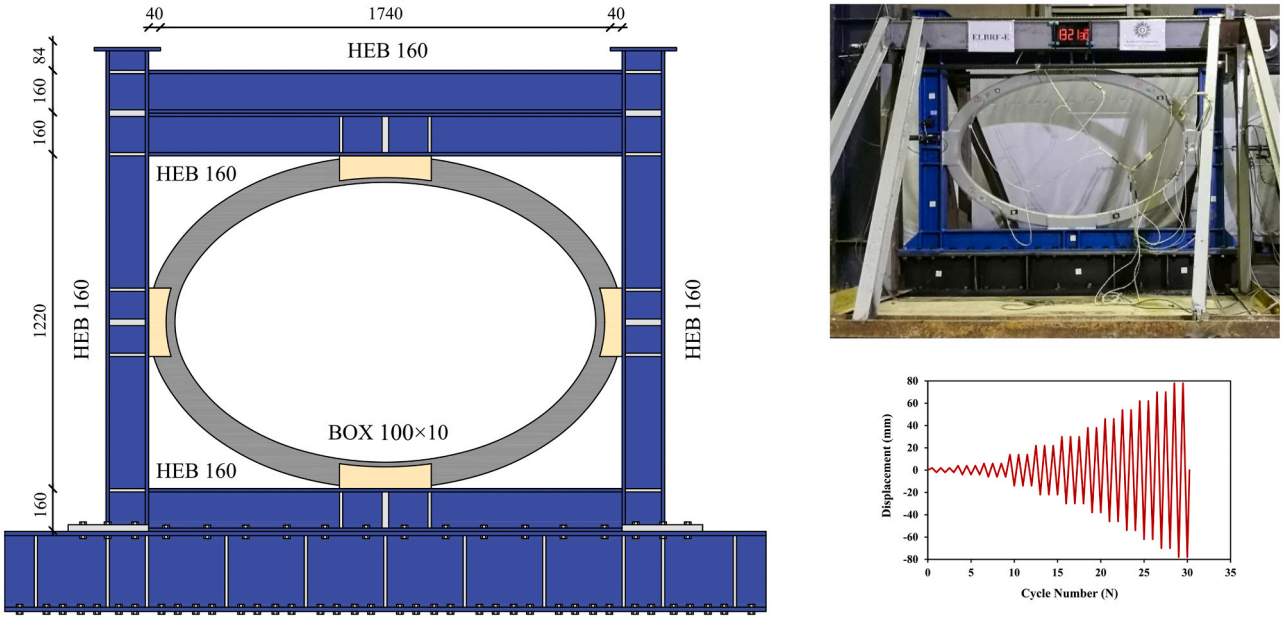

Fig. 6. Details of the ELBRF system's experimental test [72].

Table 2
Mechanical properties of steel materials from the tension coupon tests [72].

Sections	F_y $[N/mm^2]$	F_u $[N/mm^2]$	E $[N/mm^2]$	Yield strain	Hardening strain	Ultimate strain
HEB 160	355	512	203200	0.17%	1.86%	25%
BOX 100 × 10	360	551	205600	0.18%	3.28%	20%

materials' plastic behavior. The true stress-true strain curve was drawn employing the power law relationship, which is expressed as:

$$\sigma = K\varepsilon^n \tag{6}$$

where σ, ε, K, and n represent true stress, true strain, strength coefficient, and strain hardening exponent, respectively [70]. The true stress-true strain curve of S235JR steel is depicted in Fig. 5a. The study frames subjected to displacement-controlled cyclic loading were placed based on the ATC-24 loading protocol, as presented in Fig. 5b [71]. A non-linear static general analysis was performed on both bracing models, and the resulting outcomes were compared to each other.

3.2. Verification of finite element modeling

The outcomes of the experiments carried out by Jouneghani et al. on an elliptical braced resisting frame (ELBRF) were used to verify the accuracy of finite element modeling in this study. They quasi-statically loaded a single-span, single-story elliptical bracing frame with a hydraulic jack. The beam-to-column and brace-to-frame connections were considered rigid in this model [72]. Fig. 6 shows the bracing frame dimensions and cross-sections utilized for its members. In addition, the bracing frame underwent quasi-static loading using the ATC-24 loading protocol [71]. Table 2 provides the mechanical properties of the steel materials used for the cross-sections, derived from tensile coupon testing.

The finite element modelling accuracy of the bracing frame was assessed under cyclic loading employing Abaqus software. The experimental and numerical hysteresis and backbone curves of the ELBRF, along with the contour plot of von Mises stress distribution, are depicted in Fig. 7. It is clear that a close agreement is observed between the

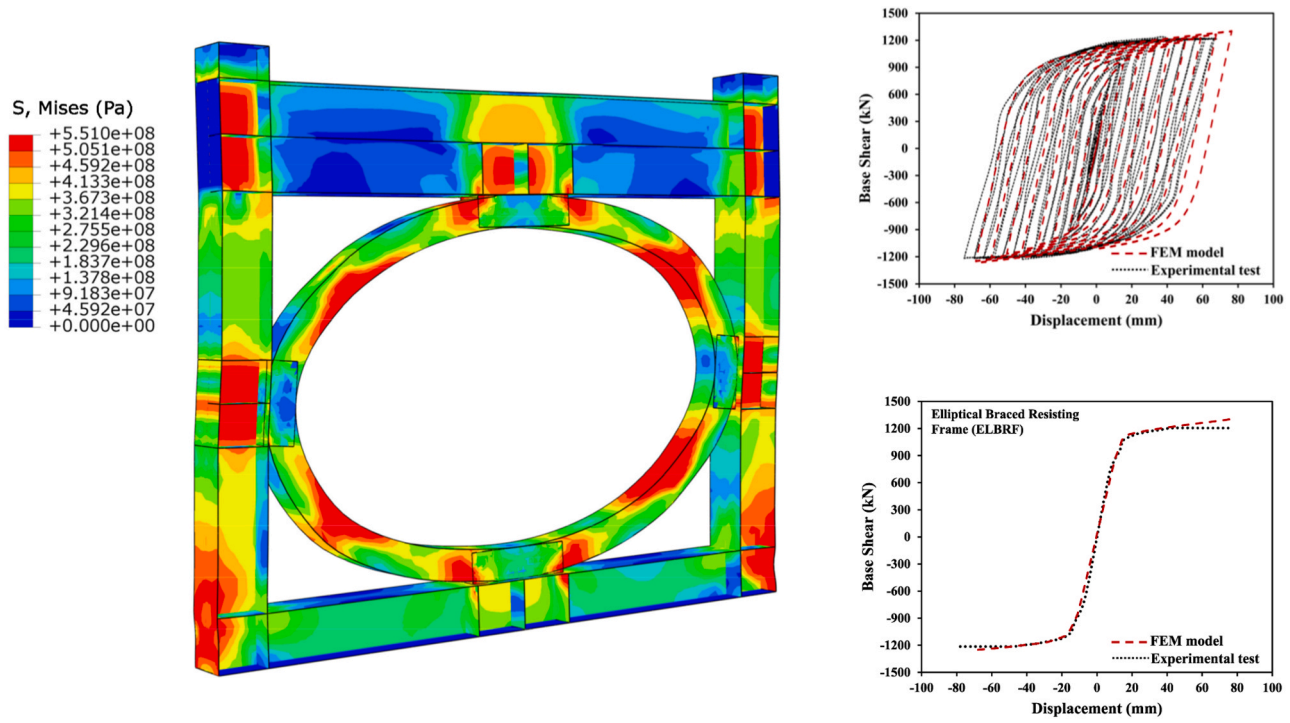

Fig. 7. Comparison of the numerical and experimental results of the ELBRF system.

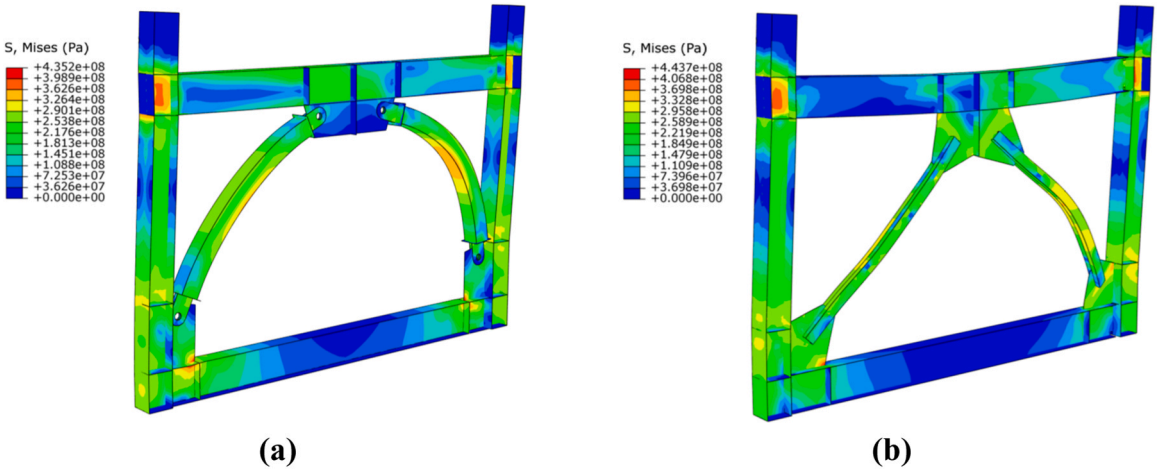

Fig. 8. Contour plots of von Mises stress distribution (in Pa); (a) HEB-MF model, (b) IVBF model.

experimental and numerical results.

3.3. Numerical study results

The contour plots of von Mises stress distribution in the HEB-MF and IVBF models are shown in Fig. 8. As depicted in this figure, the IVBF model's mid-span gusset plate experiences higher stress levels than the HEB-MF model due to the out-of-plane buckling of its bracing member. Similarly, the IVBF model encounters a higher beam mid-span deflection than the HEB-MF model because of a greater unbalanced vertical force.

Fig. 9 portrays the curves derived from analyzing two HEB-MF and IVBF bracing models, encompassing hysteresis, backbone, beam mid-span deflection, unbalanced force, and dissipated energy curves. According to Fig. 9a, the comparison of hysteresis curves reveals that as the lateral force increases in the IVBF model, the strength and stiffness initially increase and then decrease upon buckling of the bracing members. In contrast, the strength and stiffness of the HEB-MF model are not dependent; strength increases as stiffness decreases. The comparison of backbone curves in Fig. 9b demonstrates that the initial stiffness of the HEB-MF model is lower than that of the IVBF model, while its ultimate strength is greater by 59%. As shown in Fig. 9c and d, the HEB-MF model indicates a noteworthy reduction of 557% in beam mid-span deflection and 264% in unbalanced vertical force as compared to the IVBF model.

Additionally, as per Fig. 9e, the HEB-MF model exhibits a 51% increase in energy dissipation compared to the IVBF model. As a result, the comparison of outcomes discloses that employing HEB-MF systems not only effectively reduces unbalanced vertical forces and beam mid-span deflection but also enhances ultimate strength, ductility, and energy dissipation compared to IVBF systems.

4. Designing and developing HEB-MF system archetypes

In order to achieve comprehensive coverage of the structural

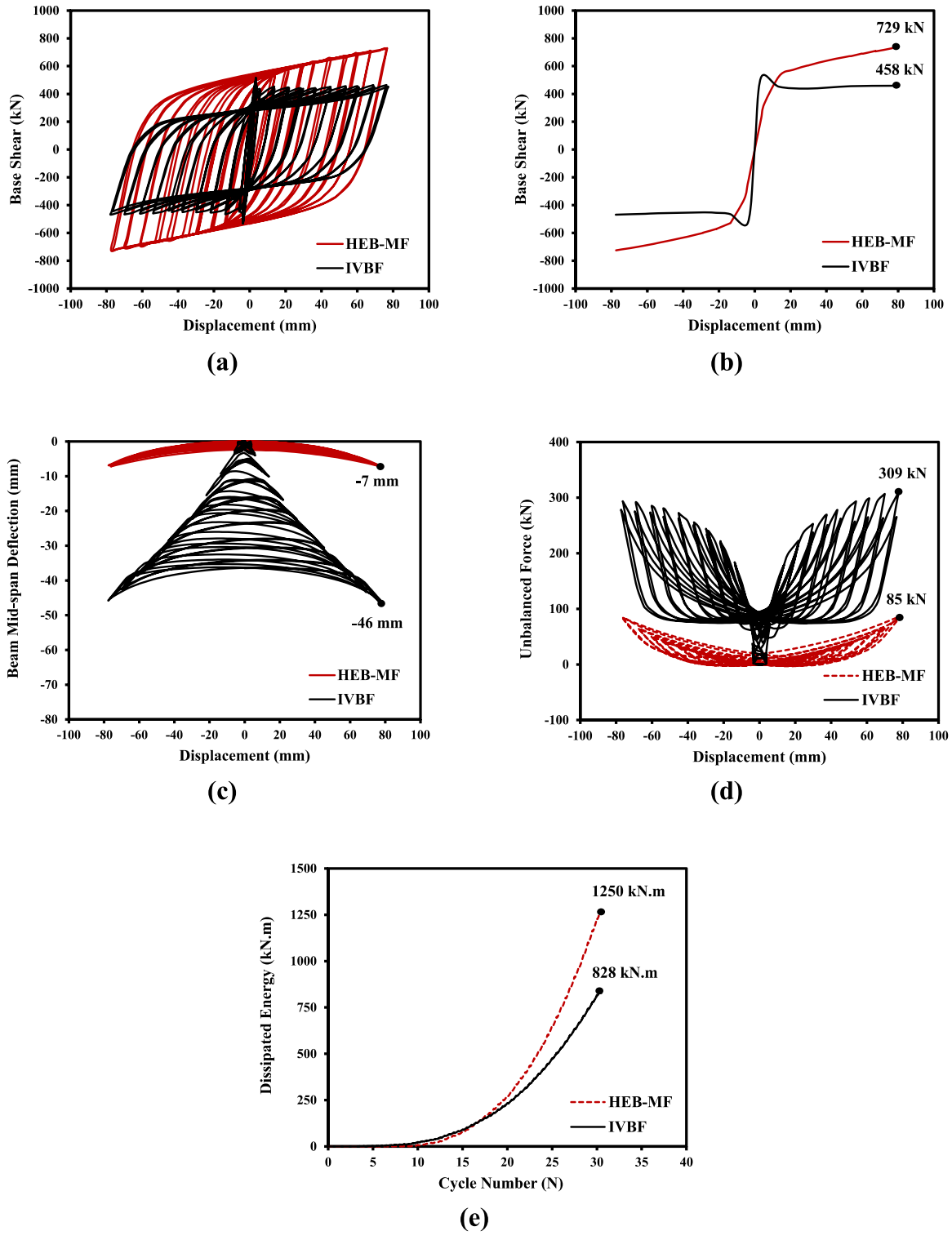

Fig. 9. Comparison of HEB-MF and IVBF models results; (a) hysteresis curves, (b) backbone curves, (c) beam mid-span deflection curves, (d) unbalanced force curves, (e) dissipated energy curves.

system's design space, it is necessary to determine and design a specified number of archetypes within the framework of the FEMA P695 procedure after selecting the intended structural system [60]. To this end, considering the key parameters influencing the structure's performance, eight archetypes with varying numbers of stories in two separate seismic design categories (SDC C_{max} and C_{min}) were selected for this study. These archetypes were classified into four performance groups (PGs) based on the period domain and different SDCs, as presented in Table 3.

As depicted in Fig. 10, the studied archetypes possess a symmetrical and regular plan with three bays per side. The length of each bay is 6 *m*, and a height of 3.2 *m* is considered for each story. The perimeter frames are also equipped with the HEB-MF system, and the bracing members are placed at their mid-bays. The archetypes are intended for residential use with an intermediate seismic importance factor . In this study, IPE cross-sections were assigned to beams and BOX cross-sections to columns and bracing members. S235JR steel grade was employed for all

Table 3
Performance groups (PGs) for assessing the HEB-MF system.

PG NO.	Archetype ID	Design load level		Period domain	Number of stories
		Gravity	Seismic		
PG-1	HEB-MF-2 H	Residential (I_e=1)	SDC C_{max}	Short	2
PG-2	HEB-MF-4 H			Long	4
	HEB-MF-6 H				6
	HEB-MF-8 H				8
PG-3	HEB-MF-2 L		SDC C_{min}	Short	2
PG-4	HEB-MF-4 L			Long	4
	HEB-MF-6 L				6
	HEB-MF-8 L				8

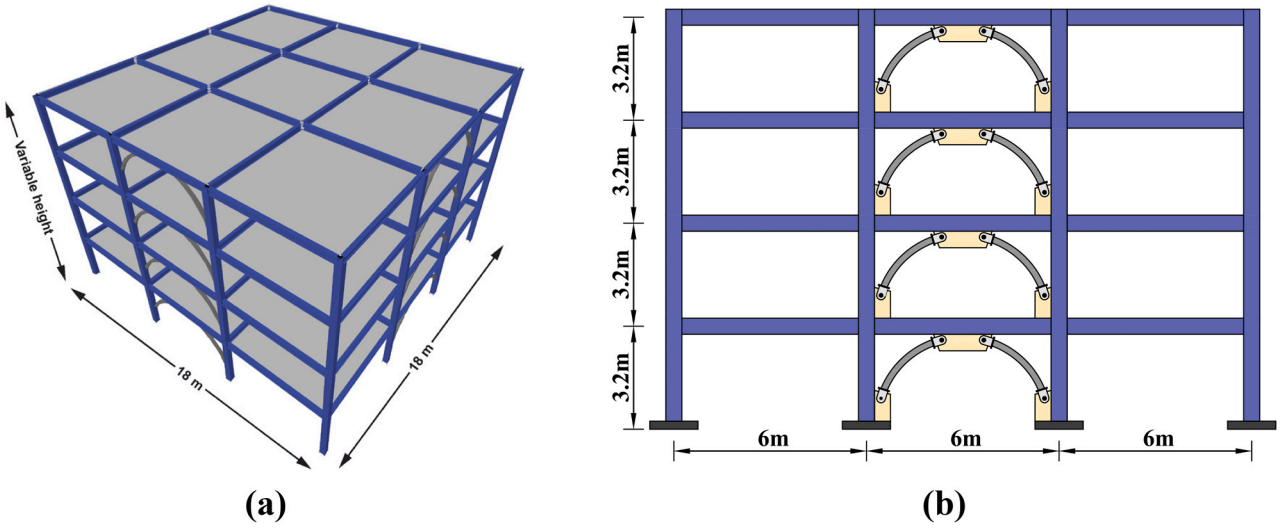

Fig. 10. HEB-MF archetypes configuration; (a) three-dimensional view, (b) bracing frame elevation view.

Table 4
Assigned gravitational loads for designing archetypes.

	Dead (kN/m^2)	Live (kN/m^2)	Wall (kN/m^2)	Partition (kN/m^2)
Roof loads	4.80	1.50	1.76	0.00
Floor loads	4.30	2.00	1.76	0.50

members as per the EN1993–1-1 standard [69]. The composite steel deck was allocated to the gravity load-resisting systems of all floors under the assumption of a rigid floor diaphragm. The gravity loads for designing archetypes were assumed based on the typical values of live and dead loads stipulated in the ASCE/SEI 7–22 standard [73]. The values assigned to gravitational dead and live loads are outlined in Table 4.

The seismic loading was carried out according to the ASCE 7–22 standard [73], with an assumed initial *R* factor of 7.5. The equivalent lateral force (ELF) method was used to analyze the archetypes within the ETABS software by considering the effects of P-Delta and the vertical earthquake. These archetypes were designed according to the ANSI/AISC 360–16 standard and the ANSI/AISC 341–16 seismic provision [74,75]. The ASCE/SEI 7–22 standard was also utilized to control stories' drift and structural stability post-design [73].

5. Non-linear modeling of HEB-MF system archetypes

In this study, two-dimensional non-linear models of HEB-MF archetypes were selected to assess the structural system's seismic performance. This choice is based on the regularity observed in the height and plan of the studied archetypes, which also aids in reducing computational costs. In order to perform non-linear modeling and analysis, these models were simulated using the OpenSees software, which adheres to the stipulated conditions in the FEMA P695 guidelines [76]. To this end, a side frame in the *x* direction was chosen from each archetype and modeled in this software, as illustrated in Fig. 11. The designed cross-sections for two-dimensional HEB-MF archetypes are listed in Table 5.

The structural mass must be appropriately shifted from a three-dimensional model to a two-dimensional model to ensure accuracy in seismic force calculations arising from dynamic analyses using ground motion records. Given the symmetric plan of the structure, the selected frames provide half of the lateral stiffness of the three-dimensional archetypes in the *x* direction. Accordingly, 50% of the overall mass of the three-dimensional archetypes, encompassing both dead loads and a portion of live loads, was extracted from the ETABS software and assigned as concentrated mass at the column element's end nodes at each story of selected frames.

Furthermore, the gravitational loads caused by the eliminated intermediate frames were transferred to the leaning columns. The complete non-linear modeling of the archetypes, accompanied by the deterioration model, specified elements for members, panel zone, and leaning column, is depicted in Fig. 12a. As shown in this figure, due to the lack of two low-cycle fatigue parameters for elliptical braces, the softening and degradation of archetype members were evaluated using the lumped-plasticity modeling approach [77]. The middle elements of the columns and beams were considered elastic, while the ends were

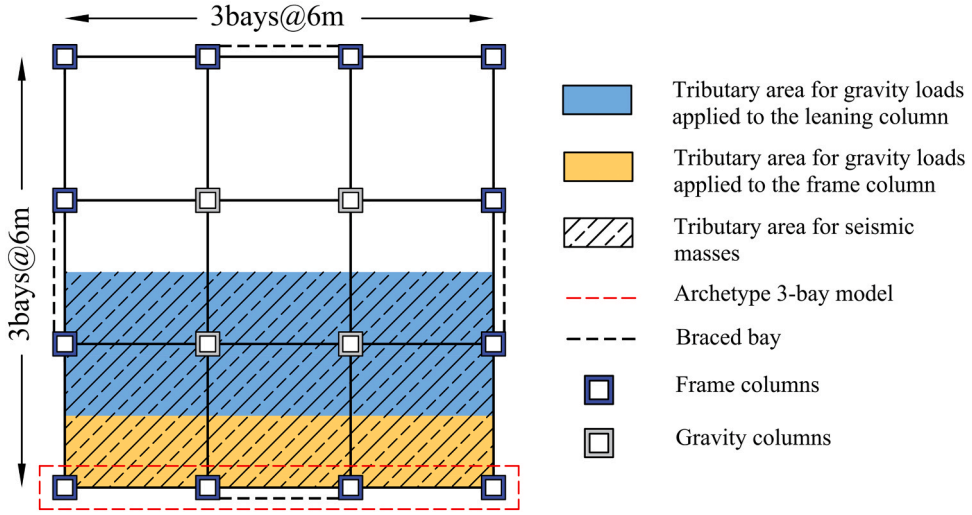

Fig. 11. Plan view of HEB-MF system archetypes.

equipped with plastic hinges. Likewise, a set of twelve elastic elements and five plastic hinges was used to enhance the modeling precision of the quarter-elliptical bracing members. The structural connections have been modeled in this study as fixed supports, and the effects of the structure-soil interaction have been ignored. A modified Ibarra-Medina-Krawinkler (ModIMK) deterioration model was integrated with a bilinear hysteretic response (Bilin material) to evaluate all members' moment-rotation behavior [78–80]. In Fig. 12b, the ModIMK model is portrayed, which consists of a number of effective parameters. These parameters are effective elastic stiffness (K_e), capping strength and associate rotation for monotonic loading (M_c and θ_c), effective yield strength and rotation (M_y and θ_y), residual strength (M_r), pre-capping rotation capacity for monotonic loading (θ_p), post-capping rotation capacity (θ_{pc}), cyclic deterioration parameter (κ) and ultimate rotation capacity (θ_u). These parameters were computed based on the findings of studies by Lignous et al. and complying with the NIST 2017b guidelines. This guideline recommends applying equations from the first cycle envelope curve for non-linear static analysis and equations related to the monotonic backbone curve for non-linear dynamic analysis [78–81]. Considering the period of the primary two modes, the Rayleigh damping model with a damping ratio of 2.5% was used for all archetypes based on the ASCE/SEI 7–22 standard's recommendation [73]. Each level's nodes were constrained in the OpenSees software using the equalDOF command to simulate the rigid floor diaphragm [76]. In this investigation, the panel zone was simulated by applying the Gupta and Krawinkler method, aiming to attain complete and exact modeling. This method encompasses the configuration illustrated in Fig. 12c, wherein the panel zone is defined by eight rigid elements and a rotational spring arranged rectangularly. The rotational spring utilizes hysteretic materials with trilinear behavior to simulate shear force-deformation behavior in the panel zone [82].

The effects of other parallel frames with the studied frame in three-dimensional space and the P-Delta effects were considered using the leaning column in OpenSees software. To achieve this, an extra bay was added to the frame, and the eliminated loads from the middle frames were applied to this bay's columns, which had been connected to the main frame through pinned connections. In this bay, rigid elements were used for the columns and truss elements for the beams. Additionally, the leaning columns were connected together by rotational springs possessing negligible stiffness to prevent moment absorption [81].

6. Non-linear modeling verification

The results of the experiments conducted by Jouneghani et al. on an elliptical braced resisting frame (ELBRF) were utilized to validate the accuracy of non-linear modeling in this section as well [72]. The bracing frame's dimensions, member cross-sections, and mechanical properties of the steel materials used for them are shown in Fig. 6 and Table 2. The bracing frame's non-linear modeling accuracy was evaluated through OpenSees software under cyclic loading. For this purpose, the concentrated plasticity method with the ModIMK deterioration model and Krawinkler's panel zone model were employed [78–82]. The ELBRF's experimental and numerical hysteresis and backbone curves were plotted and compared in Fig. 13. The examination of the curves illustrates a proper conformity between the numerical and experimental outcomes. Due to the lack of stiffener modeling in the OpenSees software, there is a tiny difference in the bracing frame's hysteresis curves and energy absorption.

7. Non-linear analyses of HEB-MF system archetypes

7.1. Non-linear static (pushover) analysis

As per FEMA P695 guidelines, non-linear static (pushover) analysis is conducted to determine the values of the period-based ductility (μ_T) and the over-strength (Ω) factors, as well as to validate and verify the seismic behavior of structural archetypes. A gravity load combination and a lateral load pattern are required to perform this analysis. In order to account for the second-order effect (P-Delta) in non-linear static analyses, FEMA P695 introduces the gravity load combination specified by Eq. (7):

$$1.05D + 0.25L \tag{7}$$

where D and L denote the nominal dead and live loads, respectively. Additionally, in accordance with this guideline, the archetypes need to undergo lateral displacement aligned with the first mode shape. Eq. (8) presents the lateral force distribution along the structure's height (F_x) for performing non-linear static analysis, where m_x represents the structure's mass at each floor level (x) and $\varphi_{1,x}$ signifies the structure's first mode at that level [60].

$$F_x \propto m_x \varphi_{1,x} \tag{8}$$

Fig. 14 demonstrates the pushover curves of the HEB-MF system archetypes. As depicted in this figure, all archetypes exhibit positive post-yield stiffness, and the post-capping strength deterioration in large deflections is attributed to considering the P-Delta effects. According to this figure, V, V_{max}, and W signify the design base shear, the maximum base shear capacity in pushover analysis, and the structure's total

Table 5
The designed cross-sections for HEB-MF system archetypes.

PG NO.	Archetype ID	Story NO.	Column		Beam	Brace
			Exterior	Interior		
PG-1	HEB-MF-2 H	1	BOX 200 × 10	BOX 200 × 10	IPE 300	BOX 100 × 10
		2	BOX 200 × 10	BOX 150 × 10	IPE 270	BOX 100 × 10
PG-2	HEB-MF-4 H	1	BOX 250 × 10	BOX 250 × 10	IPE 330	BOX 100 × 10
		2	BOX 250 × 10	BOX 250 × 10	IPE 330	BOX 100 × 10
		3	BOX 200 × 10	BOX 200 × 10	IPE 330	BOX 100 × 10
		4	BOX 200 × 10	BOX 200 × 10	IPE 300	BOX 100 × 10
	HEB-MF-6 H	1	BOX 300 × 10	BOX 300 × 10	IPE 360	BOX 120 × 12
		2	BOX 300 × 10	BOX 300 × 10	IPE 360	BOX 120 × 12
		3	BOX 250 × 10	BOX 250 × 10	IPE 360	BOX 120 × 12
		4	BOX 250 × 10	BOX 250 × 10	IPE 330	BOX 100 × 10
		5	BOX 200 × 10	BOX 200 × 10	IPE 330	BOX 100 × 10
		6	BOX 200 × 10	BOX 150 × 10	IPE 270	BOX 100 × 10
	HEB-MF-8 H	1	BOX 300 × 15	BOX 300 × 15	IPE 400	BOX 120 × 12
		2	BOX 300 × 15	BOX 300 × 15	IPE 400	BOX 120 × 12
		3	BOX 300 × 10	BOX 300 × 10	IPE 400	BOX 120 × 12
		4	BOX 250 × 10	BOX 300 × 10	IPE 360	BOX 120 × 12
		5	BOX 250 × 10	BOX 250 × 10	IPE 360	BOX 100 × 10
		6	BOX 250 × 10	BOX 250 × 10	IPE 330	BOX 100 × 10
		7	BOX 200 × 10	BOX 200 × 10	IPE 330	BOX 100 × 10
		8	BOX 200 × 10	BOX 150 × 10	IPE 300	BOX 100 × 10
PG-3	HEB-MF-2 L	1	BOX 200 × 10	BOX 150 × 10	IPE 300	BOX 100 × 10
		2	BOX 200 × 10	BOX 150 × 10	IPE 270	BOX 100 × 10
PG-4	HEB-MF-4 L	1	BOX 200 × 10	BOX 250 × 10	IPE 300	BOX 100 × 10
		2	BOX 200 × 10	BOX 200 × 10	IPE 300	BOX 100 × 10
		3	BOX 200 × 10	BOX 150 × 10	IPE 300	BOX 100 × 10
		4	BOX 200 × 10	BOX 150 × 10	IPE 270	BOX 100 × 10
	HEB-MF-6 L	1	BOX 250 × 10	BOX 250 × 10	IPE 330	BOX 100 × 10
		2	BOX 250 × 10	BOX 250 × 10	IPE 330	BOX 100 × 10
		3	BOX 200 × 10	BOX 200 × 10	IPE 330	BOX 100 × 10
		4	BOX 200 × 10	BOX 200 × 10	IPE 300	BOX 100 × 10
		5	BOX 200 × 10	BOX 150 × 10	IPE 300	BOX 100 × 10
		6	BOX 200 × 10	BOX 150 × 10	IPE 270	BOX 100 × 10
	HEB-MF-8 L	1	BOX 300 × 10	BOX 300 × 10	IPE 330	BOX 100 × 10
		2	BOX 300 × 10	BOX 300 × 10	IPE 330	BOX 100 × 10
		3	BOX 250 × 10	BOX 250 × 10	IPE 330	BOX 100 × 10
		4	BOX 250 × 10	BOX 250 × 10	IPE 330	BOX 100 × 10
		5	BOX 250 × 10	BOX 200 × 10	IPE 330	BOX 100 × 10
		6	BOX 200 × 10	BOX 200 × 10	IPE 300	BOX 100 × 10
		7	BOX 200 × 10	BOX 150 × 10	IPE 300	BOX 100 × 10
		8	BOX 200 × 10	BOX 150 × 10	IPE 270	BOX 100 × 10

weight, respectively. C_s denotes the seismic response coefficient in ELF analysis and is calculated based on ASCE/SEI 7–22 for each archetype [73]. δ_u represents the ultimate displacement of the structure's roof resulting from a reduction of 20% in the maximum base shear capacity. $\delta_{y,eff}$ signifies the effective yield displacement of the structure's roof and is calculated utilizing Eq. (9):

$$\delta_{y,eff} = C_0 \frac{V_{max}}{W} \left[\frac{g}{4\pi^2}\right] (\max(T, T_1))^2 \tag{9}$$

where g, T, and T_1 denote the gravitational acceleration, the structure's fundamental period as per ASCE/SEI 7–22 standard relationships, and the structure's fundamental vibration period as determined by the eigenvalue analysis.

Furthermore, C_0 indicates the first-mode excitation coefficient at the structure's roof level. This coefficient is computed with regard to the ASCE/SEI 41–06 standard through Eq. (10):

$$C_0 = \varphi_{1,r} \frac{\sum_{x=1}^{N} m_x \varphi_{1,x}}{\sum_{x=1}^{N} m_x {\varphi_{1,x}}^2} \tag{10}$$

where m_x, and $\varphi_{1,x}$ signify the structure's mass and the structure's first mode at each floor level (x). N designates the total number of floors, and $\varphi_{1,r}$ denotes the structure's first mode at the roof level [73,83]. The Ω factor is computed using Eq. (11), while the μ_T factor is determined through Eq. (12) based on FEMA P695 procedures.

$$\Omega = \frac{V_{max}}{V} = \frac{V_{max}}{C_s W} \tag{11}$$

$$\mu_T = \frac{\delta_u}{\delta_{y,eff}} \tag{12}$$

Table 6 provides a summary of the results derived from the HEB-MF system archetypes' pushover curves and the aforementioned equations. Regarding the outcomes in both SDCs, the 2-story HEB-MF archetypes have the highest Ω factor, while the 8-story HEB-MF archetypes have the highest μ_T factor.

7.2. Incremental dynamic analysis (IDA)

In order to quantify the SPFs of HEB-MF systems conforming to FEMA P695 procedures, the median collapse intensity $(\widehat{S}_{CT})$ values must first be determined for all archetypes using incremental dynamic analysis (IDA). Selecting appropriate intensity measure (IM) and damage measure (DM) parameters is essential in IDA analysis. A suitable IM reduces the dispersion of structure responses under different earthquakes, enhancing accuracy in statistical approximations for these responses. According to the standard procedure in numerous other studies and the FEMA P695 recommendations, this parameter was considered equivalent to the first mode-5% damped spectral acceleration, $S_a\,(T_1,\ 5\%)$. Likewise, the DM parameter was considered equivalent to the maximum inter-story drift ratio (MIDR). As per FEMA P695, the collapse

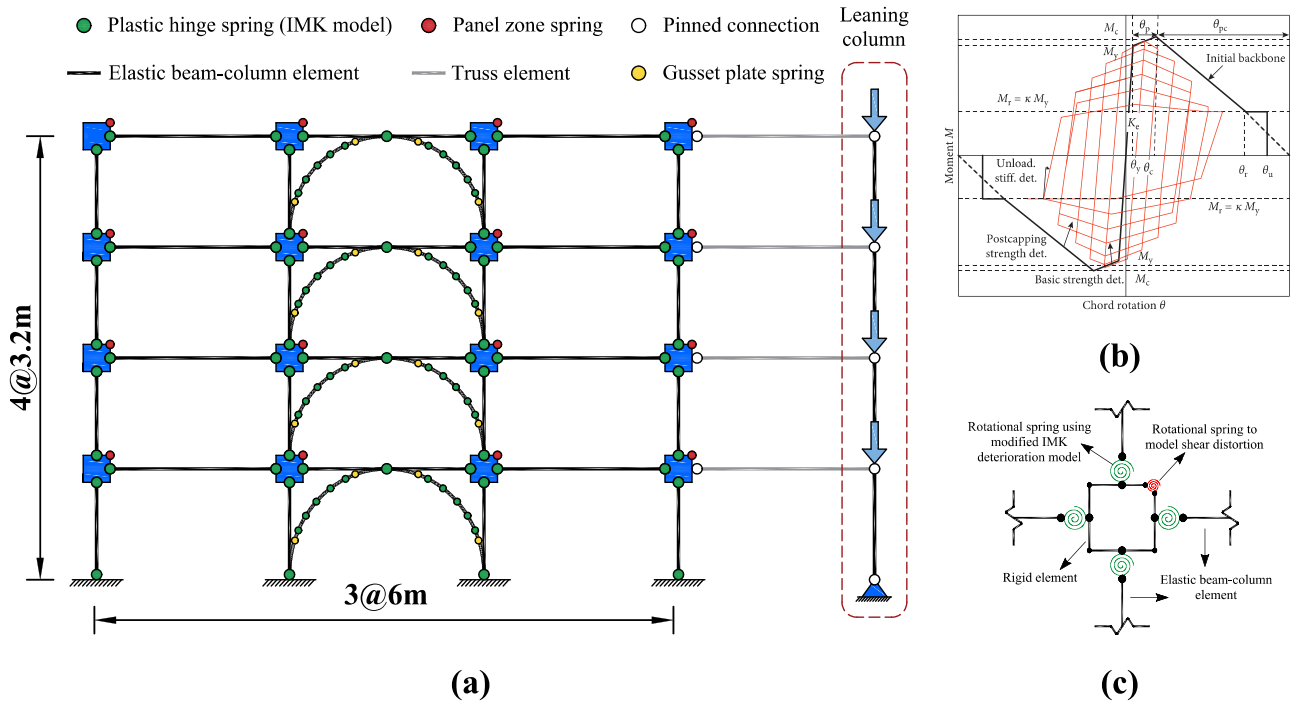

Fig. 12. OpenSees non-linear modeling; (a) HEB-MF system archetypes, (b) components of Krawinkler's panel zone model, (c) ModIMK deterioration model.

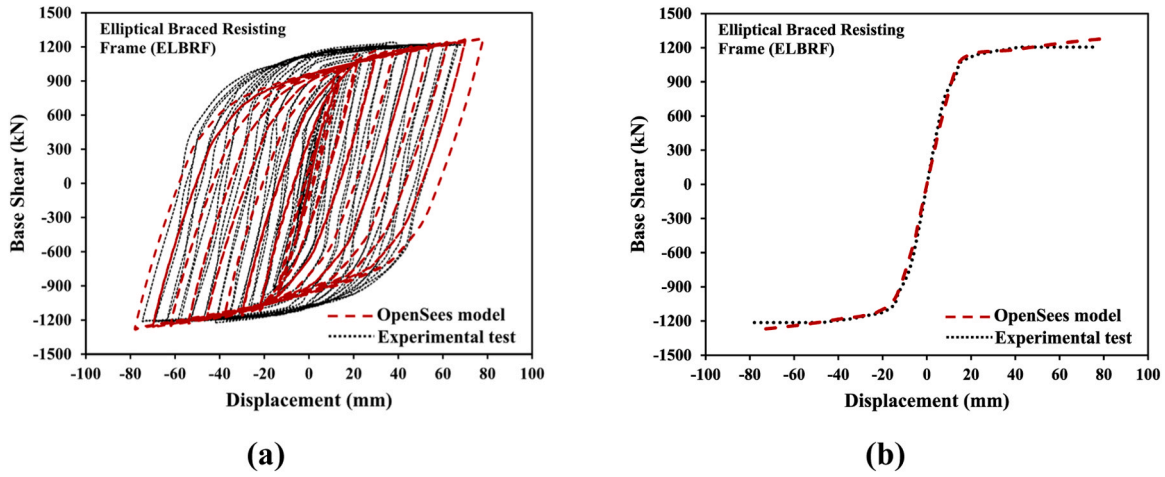

Fig. 13. Numerical model vs. experimental test of the ELBRF system; (a) hysteresis curves, (b) backbone curves.

criteria for IDA analysis have been considered to encompass the reduction of the IDA curve's slope to 20% of the initial elastic slope, dynamic instability, a significant increase in inter-story drift, and non-simulated fracture [60]. The FEMA P695 assessment method employs near-field ground motion (NFGM) and far-field ground motion (FFGM) records to estimate archetypes' seismic responses in non-linear dynamic analysis. The FFGM records, comprising 22 pairs of horizontal records positioned 10 *km* or more from the fault rupture line, estimate the seismic performance of archetypes designed under SDC B, C, and D. In contrast, the NFGM records, including 28 pairs of horizontal records located less than 10 *km* from the fault rupture line, assess seismic performance for archetypes designed under SDC E in special research [60–65]. Therefore, only FFGM records were used to evaluate the archetypes' seismic performance in this study. Table 7 lists selected FFGM records, whose acceleration and median response spectra are depicted in Fig. 15. It is impossible to specify the required steps for achieving collapse during the IDA analysis, and the number of such analyses may be considerable owing to the time-consuming nature of reaching the collapse brink. In order to confront this challenge, the advanced "hunt and fill" algorithm was implemented, aimed at minimizing the number of steps needed to reach the collapse point [84].

The median collapse intensity ($\widehat{S}_{CT}$) values, indicating the point where half of the records lead to structural collapse, are extracted from IDA curves. Then, each structure's collapse margin ratio (CMR) values are computed through Eq. (13) in conformity with FEMA P695:

$$CMR = \frac{\widehat{S}_{CT}}{S_{MT}} \tag{13}$$

where S_{MT} signifies the maximum considered earthquake (MCE) ground motion intensity, determined by the structure's fundamental period (T) for different SDCs as outlined in FEMA P695 [60]. Fig. 16 shows the HEB-MF system archetypes' IDA curves with 16%, 50%, and 84% fractile curves subjected to FFGM records. As indicated in this figure, the increase in the number of archetypes' stories in both SDC C_{max} and C_{min}

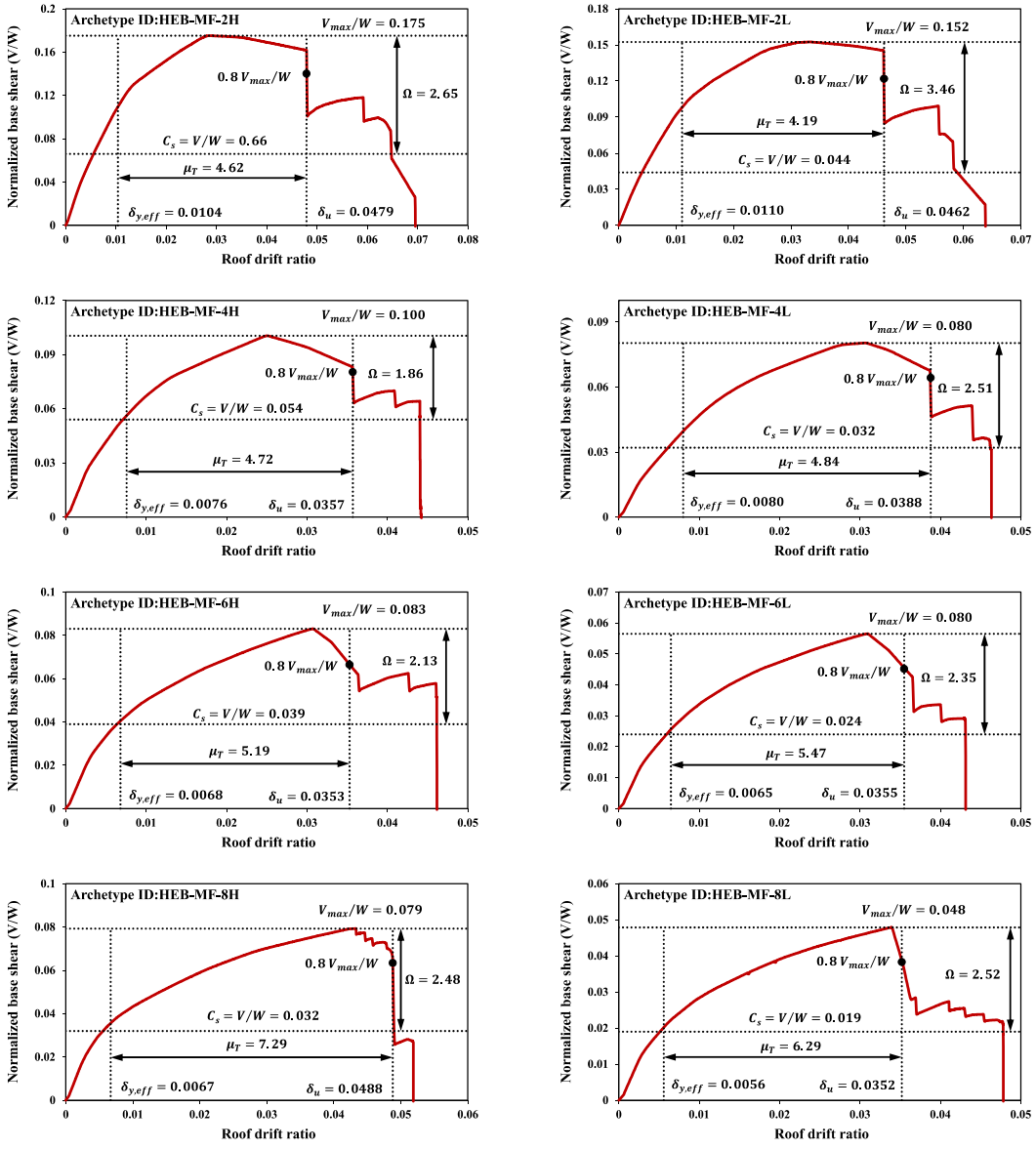

Fig. 14. Pushover curves of the HEB-MF system archetypes.

Table 6
Results of HEB-MF system archetypes' modal and pushover analyses.

PG NO.	Archetype ID	$T(s)$	T_1/T	V_{max}/W	C_s	C_0	$\delta_{y,eff}$ (%)	δ_u (%)	μ_T	Ω	Ω_{ave}
PG-1	HEB-MF-2H	0.29	3.86	0.175	0.066	1.216	1.038	4.79	4.62	2.65	2.65
PG-2	HEB-MF-4H	0.49	3.52	0.100	0.054	1.304	0.756	3.57	4.72	1.86	2.16
	HEB-MF-6H	0.67	3.19	0.083	0.039	1.387	0.680	3.53	5.19	2.13	
	HEB-MF-8H	0.82	3.02	0.079	0.032	1.417	0.669	4.88	7.29	2.48	
PG-3	HEB-MF-2L	0.32	3.88	0.152	0.044	1.208	1.103	4.62	4.19	3.46	3.46
PG-4	HEB-MF-4L	0.54	3.67	0.080	0.032	1.306	0.801	3.88	4.84	2.51	2.46
	HEB-MF-6L	0.74	3.47	0.056	0.024	1.347	0.649	3.55	5.47	2.35	
	HEB-MF-8L	0.92	3.21	0.048	0.019	1.381	0.560	3.52	6.29	2.52	

has reduced the $\widehat{S}_{CT}$ value.

To consider the influences of frequency content and statistical discrepancies among the utilized records, the CMR is modified by the spectral shape factor (SSF), and the adjusted collapse margin ratio (ACMR) is elicited for each archetype through Eq. (14) [85,86]. The μ_T factor and T (fundamental period) are used to select this factor for each structure, relying on the tables presented in FEMA P695 [60].

$$ACMR = CMR \times SSF \tag{14}$$

There are multiple sources of uncertainty affecting the distribution of collapse capacity. As per FEMA P695, modeling uncertainty (β_{MDL}), test data uncertainty (β_{TD}), design requirements uncertainty (β_{DR}), and record-to-record uncertainty (β_{RTR}) significantly impact the seismic assessment of structures. Values of 0.1, 0.2, 0.35, or 0.5 are individually

Table 7
Summary of FFGM records recommended by FEMA P695 [60].

ID No.	Event name	Year	Magnitude	Station	Site class (NEHRP)	PGA_{max} (g)	$PGV_{max}(cm/s)$
1	Northridge	1994	6.7	Beverly hills	D	0.52	63
2	Northridge	1994	6.7	Canyon country-WLC	D	0.48	45
3	Duzce, Turkey	1999	7.1	Bolu	D	0.82	62
4	Hector Mine	1999	7.1	Hector	C	0.34	42
5	Imperial valley	1979	6.5	El Centro array # 11	D	0.38	33
6	Imperial valley	1979	6.5	Delta	D	0.35	42
7	Kobe, Japan	1995	6.9	Nishi-Akashi	C	0.51	37
8	Kobe, Japan	1995	6.9	Shin-Osaka	D	0.24	38
9	Kocaeli, Turkey	1999	7.5	Duzce	D	0.36	59
10	Kocaeli, Turkey	1999	7.5	Arcelik	C	0.22	40
11	Landers	1992	7.3	Yermo Fire Station	D	0.24	52
12	Landers	1992	7.3	Coolwater	D	0.42	42
13	Loma Prieta	1989	6.9	Capitola	D	0.53	35
14	Loma Prieta	1989	6.9	Gilroy Array # 3	D	0.56	45
15	Manjil, Iran	1990	7.4	Abbar	C	0.51	54
16	Superstition Hills	1987	6.5	El Centro Imp. Co. Cent	D	0.36	46
17	Superstition Hills	1987	6.5	Poe Road	D	0.45	36
18	Cape Mendocino	1992	7.0	Rio dell overpass	D	0.55	44
19	Chi-Chi Taiwan	1999	7.6	CHY101	D	0.44	115
20	Chi-Chi Taiwan	1999	7.6	TCU045	C	0.51	39
21	San Fernando	1971	6.6	LA-Hollywood Stor FF	D	0.21	19
22	Friuli, Italy	1976	6.5	Tolmezzo	C	0.35	31

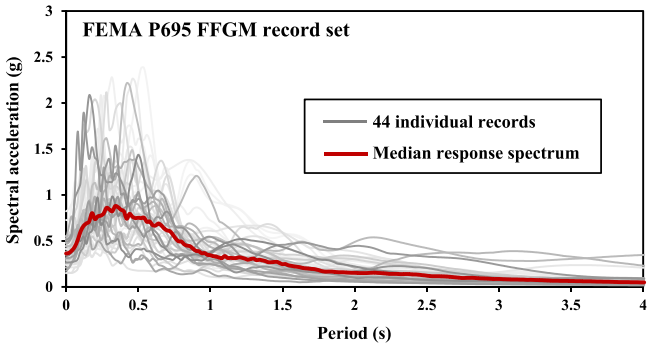

Fig. 15. Acceleration response spectra of the FEMA P695 FEGM records [60].

assigned to the β_{MDL}, β_{TD}, and β_{DR} uncertainties, contingent upon their associated quality levels. These values are related to specific quality levels: 0.1 for quality level A (superior), 0.2 for quality level B (good), 0.35 for quality level C (fair), and 0.5 for quality level D (poor). In contrast, the β_{RTR} uncertainty relies on the value of the μ_T factor and is computed through Eq. (15):

$$0.2 \le \beta_{RTR} = 0.1 + 0.1\mu_T \le 0.4 \tag{15}$$

Regarding the archetypes' characteristics and their modeling requirements, quality level A (equal to 0.2) was appointed in this study for the β_{MDL}, β_{TD}, and β_{DR} uncertainties, and the β_{RTR} uncertainty was obtained using Eq. (15).

Archetypes' seismic performance is assessed using the standard deviation of the total collapse uncertainty (β_{TOT}) due to the uncertainties' statistical independence, as outlined in Eq. (16):

$$\beta_{TOT} = \sqrt{{\beta_{MDL}}^2 + {\beta_{TD}}^2 + {\beta_{DR}}^2 + {\beta_{RTR}}^2} \tag{16}$$

The fragility curves demonstrate the probability of structural collapse for various earthquake intensities and can ascertain the probability of collapse occurrence for each level of spectral acceleration. To draw these curves, the initial step involves determining collapse-associated spectral accelerations for various records using IDA analysis. The probability of exceeding different spectral accelerations is then computed by applying a probability cumulative distribution function (CDF) such as the normal distribution function to this dataset, and the fragility curve is drawn [60]. Fig. 17 depicts the HEB-MF system archetypes' fragility curves under FFGM records, considering uncertainties. In the two dashed fragility curves, β_{RTR} and β_{TOT} were considered the standard deviation parameters in the log-normal distribution. Also, the solid fragility curve (shifted fragility curve) was delineated by multiplying the fragility curve with the standard deviation parameter β_{TOT} in SSF. As illustrated in Fig. 17, when the standard deviation amount rises, the slope of fragility curves experiences a reduction, resulting in an increased collapse probability of S_{MT}.

8. Quantifying the SPFs of HEB-MF systems

8.1. The response modification factor (R)

In order to confirm the assumed R factor according to the FEMA P695 guidelines, the collapse probability for each archetype should be under 10%, and for each performance group, it should be under 20% under MCE earthquakes.

In FEMA P695, the expressed probable objectives are indirectly assessed through the acceptable values of ACMR. Hence, the suggested R factor value is deemed acceptable if Eqs. (17) and (18) are fulfilled [60].

$$ACMR_i \ge ACMR_{20\%} \tag{17}$$

$$\overline{ACMR_i} \ge ACMR_{10\%} \tag{18}$$

where $ACMR_i$ and $\overline{ACMR_i}$ signify the adjusted collapse margin ratio value for each archetype and the average value of the adjusted collapse margin ratio for each performance group, respectively. Additionally, $ACMR_{10\%}$ and $ACMR_{20\%}$ represent the acceptable values of the adjusted collapse margin ratio. These values are determined based on β_{TOT}, as outlined in FEMA P695 guidelines [60]. The ACMR values of the HEB-MF system archetypes are compared in Fig. 18. This figure illustrates that the ACMR value decreases as the number of stories increases, except for the 8-story archetype in SDC C_{max}. This difference could be due to the drift control as per ASCE/SEI 7–22 and the more robust consideration of cross-sections (specifically beams) for the 8-story archetype [73].

Table 8 provides a summary of the achieved outcomes for HEB-MF systems in comparison with the acceptable values specified in FEMA P695. Based on the results, the two conditions outlined in Eqs. (17) and (18) have been met for all HEB-MF system archetypes. Therefore, the assumed response modification factor $(R = 7.5)$ is corroborated. Moreover, there is no necessity to augment the R factor given the

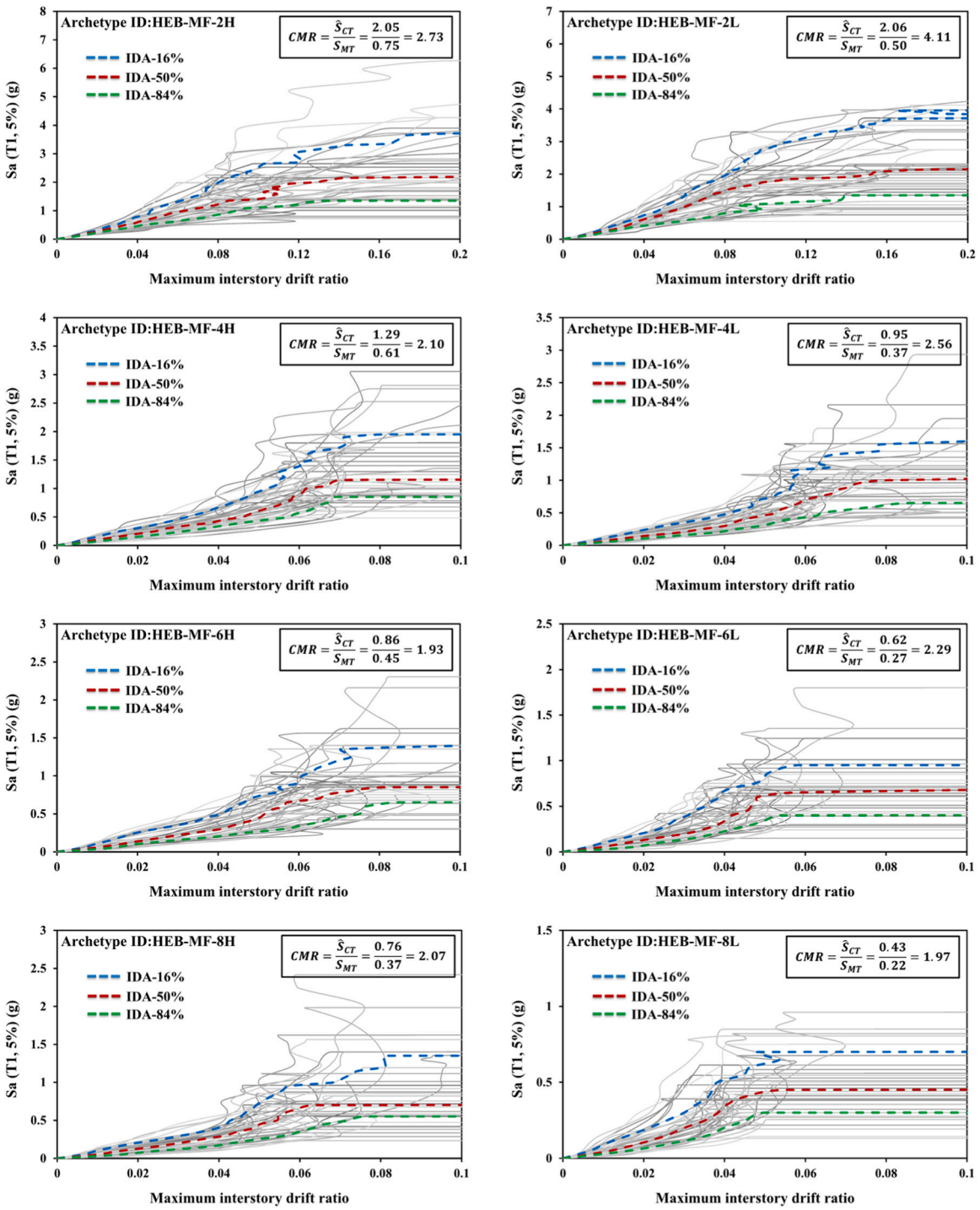

Fig. 16. IDA curves of the HEB-MF system archetypes under FFGM records.

proximity of the $\overline{ACMR}$ value of PG-2 to $ACMR_{10\%}$. It is worth mentioning that in this study, the R factor of HEB-MF systems was assumed to be 6.5 initially and then increased to 7. Due to the fulfillment of the two aforementioned conditions with a significant margin for these values, the R factor increased, and ultimately, a R factor of 7.5 was selected for HEB-MF systems.

8.2. *The over-strength factor* (Ω)

According to FEMA P695, the first step in determining structural systems' over-strength factor (Ω) is to calculate the Ω factor values for performance groups by averaging the Ω factors obtained from archetypes. Then, the maximum Ω factor among the performance groups is selected as the Ω factor for the intended structural system. Aligned with FEMA P695 guidelines, this value should stay below 1.5 times the structural system's R factor and 3, and it should be rounded conservatively to 0.5 unit intervals [60]. Based on the pushover analysis outcomes detailed in Table 6, PG-3 has the maximum value of the Ω factor, with a value of 3.46. Accordingly, the determined over-strength factor (Ω) for designing HEB-MF systems is 3.

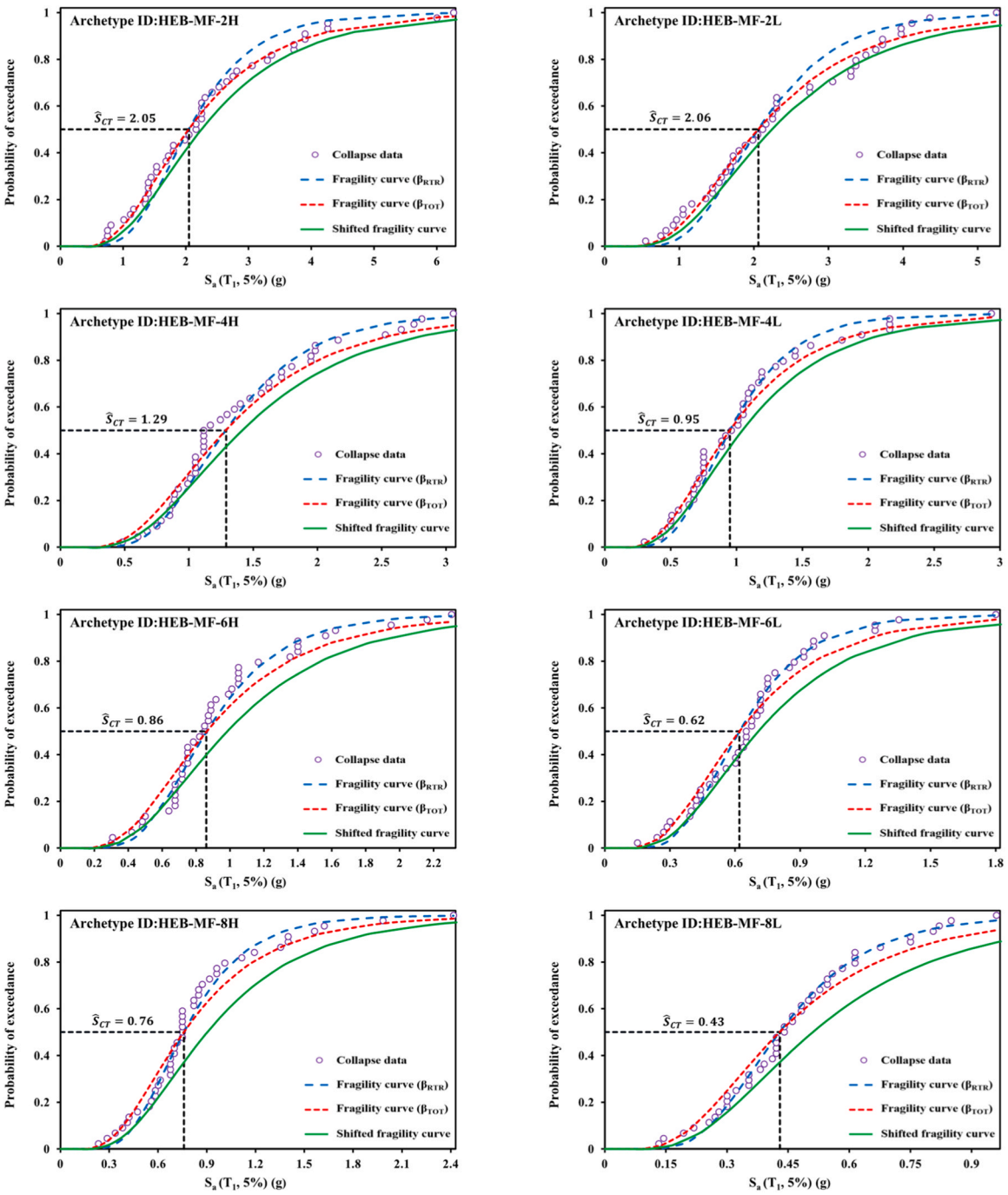

Fig. 17. Fragility curves of the HEB-MF system archetypes under FFGM records.

8.3. *The deflection amplification factor* (C_d)

Conforming to FEMA P695, a direct relationship exists between the R factor and the deflection amplification factor (C_d) [60]. Therefore, this factor is determined by dividing the ultimate R factor by the B_I coefficient, as per Eq. (19):

$$C_d = \frac{R}{B_I} \tag{19}$$

The B_I coefficient value relies on the structural system's effective damping (β_I) under examination. As outlined by ASCE/SEI 7–22 [73], the B_I coefficient is determined according to Table 9 and is calculated to equal 0.83 for a 2.5% of critical damping through linear interpolation. In accordance with FEMA P695 guidelines, this value can be conservatively considered equal to 1.0 (equivalent to 5% of critical damping). Aligning the C_d factor with the R factor is based on the Newmark rule, which assumes that the inelastic displacement is nearly equal to the elastic displacement at the roof. Research findings have demonstrated that this assumption is appropriate for systems with 5% of critical damping and fundamental periods, T, greater than the transition period, T_s (long-period systems) [60]. Consequently, the specified deflection amplification factor for designing HEB-MF systems is also considered to be 7.5.

9. Conclusions

This study proposed a novel system called the half-elliptic-braced steel moment frame (HEB-MF) to mitigate unbalanced vertical force

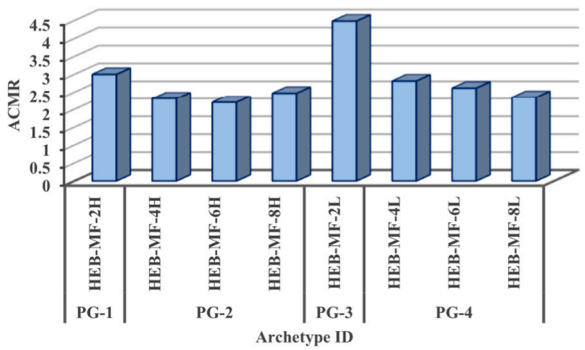

Fig. 18. Comparison of the HEB-MF system archetypes' ACMR values.

and beam deflection in chevron or inverted V-braced frames (IVBFs). Initially, this bracing system was modeled using Abaqus software and subjected to displacement-controlled cyclic loading based on the ATC-24 loading protocol. Compared to the IVBF system, the hysteresis curves, energy dissipation, unbalanced force, and beam mid-span deflection of this system were examined. Subsequently, the seismic performance factors (SPFs) of HEB-MFs were determined according to the FEMA P695 procedure. To this end, eight three-dimensional archetypes with different numbers of stories were designed in two distinct seismic design categories (SDC C_{max} and C_{min}) using assumed SPFs. Non-linear models of each archetype were constructed employing the lumped-plasticity modeling approach in OpenSees software. Non-linear static (pushover) analysis was conducted to validate the non-linear modeling and calculate the period-based ductility (μ_T) and over-strength factor (Ω) per archetype. Afterward, incremental dynamic analysis (IDA) was performed under 44 far-field ground motion (FFGM) records to assess the collapse capacity of archetypes and compute the adjusted collapse margin ratio (ACMR). The main conclusions of this study are as follows:

- HEB-MF systems reduce the probability of the first soft-story and overall building instability due to hardening at large deformations and symmetric cyclic behavior.
- In the IVBF model, as the lateral force increases, strength and stiffness initially increase and then decrease upon the buckling of the bracing members. Conversely, in the HEB-MF model, strength and stiffness are not dependent; strength increases as stiffness decreases.
- The initial stiffness of the HEB-MF model is lower than that of the IVBF model, while its ultimate strength is greater by 59%. Additionally, the HEB-MF model demonstrates a 51% increase in energy dissipation compared to the IVBF model.
- The HEB-MF model exhibits a notable reduction of 557% in beam mid-span deflection and 264% in unbalanced vertical force compared to the IVBF model.
- In SDC C_{max} and C_{min}, the 2-story HEB-MF archetypes possess the maximum Ω factor, while the 8-story HEB-MF archetypes possess the maximum μ_T factor.
- The ACMR value decreases as stories increase, except for the 8-story archetype in SDC C_{max}. This exception is due to using stronger cross-sections in line with the ASCE/SEI 7-22 standard to control drift.
- The increase in standard deviation (total uncertainty) reduces the slope of fragility curves and raises the probability of collapse at the MCE ground motion intensity (S_{MT}).
- The results indicate that HEB-MF systems' assumed response modification factor (R) fulfills FEMA P695 requirements. Therefore, the R factor of 7.5 is suitable for designing HEB-MF systems.
- Regarding the pushover analysis outcomes, PG-3 has the maximum over-strength factor (Ω) value, with a value of 3.46. Hence, the appropriate Ω factor for designing HEB-MF systems is 3.
- Conforming to FEMA P695, if the effective damping of a system is approximately 5% of the critical damping, the deflection amplification factor (C_d) is equal to the R factor. Accordingly, the proper C_d factor for designing HEB-MF systems is 7.5.

The present study revealed that using the HEB-MF system instead of the IVBF system not only reduces the unbalanced vertical force and beam mid-span deflection but also enhances energy dissipation due to increased ductility. Additionally, this bracing system improves seismic performance due to its elliptical geometry. Consequently, it could serve as an ideal replacement for IVBF systems.

CRediT authorship contribution statement

Nader Fanaie: Validation, Supervision, Project administration, Methodology, Conceptualization. **Alireza Shirpour:** Writing – review & editing, Writing – original draft, Software, Resources, Investigation, Data curation.

Table 9
Damping coefficient [73].

Effective damping, β_I (percentage of critical)	Damping coefficient, B_I
≤2	0.8
5	1.0
10	1.2
20	1.5
30	1.8
40	2.1
50	2.4
60	2.7
70	3.0
80	3.3
90	3.6
≥100	4.0

Table 8
ACMRs of HEB-MF archetypes in comparison to acceptable FEMA P695 values.

PG NO.	Archetype ID	S_{MT} (g)	$\widehat{S}_{CT}$	*CMR*	*SSF*	*ACMR*	$ACMR_{20\%}$	$ACMR_{10\%}$	Pass/Fail
PG-1	HEB-MF-2H	0.75	2.05	2.73	1.10	3.00	1.56		Pass
	Mean of performance groupe					3.00		1.96	Pass
PG-2	HEB-MF-4H	0.61	1.29	2.10	1.10	2.31	1.56		Pass
	HEB-MF-6H	0.45	0.86	1.93	1.14	2.20	1.56		Pass
	HEB-MF-8H	0.37	0.76	2.07	1.19	2.47	1.56		Pass
	Mean of performance groupe					2.33		1.96	Pass
PG-3	HEB-MF-2L	0.50	2.06	4.11	1.09	4.48	1.56		Pass
	Mean of performance groupe					4.48		1.96	Pass
PG-4	HEB-MF-4L	0.37	0.95	2.56	1.10	2.82	1.56		Pass
	HEB-MF-6L	0.27	0.62	2.29	1.14	2.62	1.56		Pass
	HEB-MF-8L	0.22	0.43	1.97	1.19	2.35	1.56		Pass
	Mean of performance groupe					2.59		1.96	Pass

Declaration of Competing Interest

The authors certify that they have no affiliations with or involvement in any organization or entity with any financial interest (such as employment, patent-licensing arrangements, etc.), or non-financial interest (such as personal or professional relationships, affiliations, knowledge or beliefs) in the subject matter discussed in this manuscript.

Data availability

Data will be made available on request.

References

[1] Zheng L, Dou S, Zhang C, Wang W, Ge H, Ma L, et al. Seismic performance of different chevron braced frames. J Constr Steel Res 2023;200:107680. https://doi.org/10.1016/j.jcsr.2022.107680.

[2] Tan Q, Lehman DE, Roeder CW, Berman JW, Sen AD, Wu B. Design-parameter study on seismic performance of chevron-configured SCBFs with yielding beams. J Constr Steel Res 2021;179:106561. https://doi.org/10.1016/j.jcsr.2021.106561.

[3] Roeder CW, Sen AD, Asada H, Ibarra SM, Lehman DE, Berman JW, et al. Inelastic behavior and seismic design of multistory chevron-braced frames with yielding beams. J Constr Steel Res 2020;167:105817. https://doi.org/10.1016/j.jcsr.2019.105817.

[4] Sen AD, Roeder CW, Berman JW, Lehman DE, Li C-H, Wu A-C, et al. Experimental Investigation of Chevron Concentrically Braced Frames with Yielding Beams. J Struct Eng 2016;142:04016123. https://doi.org/10.1061/(asce)st.1943-541x.0001597.

[5] Aydenlou RM. Seismic rehabilitation methods for existing buildings. Elsevier; 2020. https://doi.org/10.1016/C2018-0-05546-2.

[6] Roeder CW, Sen AD, Terpstra C, Ibarra SM, Liu R, Lehman DE, et al. Effect of beam yielding on chevron braced frames. J Constr Steel Res 2019;159:428–41. https://doi.org/10.1016/j.jcsr.2019.04.044.

[7] Sen AD, Roeder CW, Lehman DE, Berman JW. Nonlinear modeling of concentrically braced frames. J Constr Steel Res 2019;157:103–20. https://doi.org/10.1016/j.jcsr.2019.02.007.

[8] Wijesundara KK, Nascimbene R, Rassati GA. Evaluation of the seismic performance of suspended zipper column concentrically braced steel frames. J Constr Steel Res 2018;150:452–61. https://doi.org/10.1016/j.jcsr.2018.09.003.

[9] Yang CS, Leon RT, DesRoches R. Design and behavior of zipper-braced frames. Eng Struct 2008;30:1092–100. https://doi.org/10.1016/j.engstruct.2007.06.010.

[10] Khatib I.F., Mahin S.A., Pister K.S. Seismic behavior of concentrically braced steel frames. Earthquake Engineering Research Center, University of California Berkeley …; 1988.

[11] Li H, Zhang W, Zeng L. Seismic assessment of chevron braced frames with differently designed beams. Structures 2023;49:1028–43. https://doi.org/10.1016/j.istruc.2023.02.002.

[12] D'Aniello M, Costanzo S, Landolfo R. The influence of beam stiffness on seismic response of chevron concentric bracings. J Constr Steel Res 2015;112:305–24. https://doi.org/10.1016/j.jcsr.2015.05.021.

[13] Afsar Dizaj E, Fanaie N, Zarifpour A. Probabilistic seismic demand assessment of steel frames braced with reduced yielding segment buckling restrained braces. Adv Struct Eng 2018;21:1002–20. https://doi.org/10.1177/1369433217737115.

[14] Kim J, Choi H. Behavior and design of structures with buckling-restrained braces. Eng Struct 2004;26:693–706. https://doi.org/10.1016/j.engstruct.2003.09.010.

[15] Garjan RS, Fanaie N. Seismic behaviour assessment of eccentrically split-X braced frames. Sci Iran 2021;28:65–84. https://doi.org/10.24200/SCI.2019.50655.1804.

[16] Kumar PCA, Sahoo DR, Kumar A. Seismic response of concentrically braced frames with staggered braces in split-x configurations. J Constr Steel Res 2018;142:17–30. https://doi.org/10.1016/j.jcsr.2017.12.005.

[17] Lacerte M, Tremblay R. Making use of brace overstrength to improve the seismic response of multistorey split-X concentrically braced steel frames. Can J Civ Eng 2006;33:1005–21. https://doi.org/10.1139/L06-035.

[18] Kachooee A, Kafi MA. A suggested method for improving post buckling behavior of concentric braces based on experimental and numerical studies. Structures 2018;14:333–47. https://doi.org/10.1016/j.istruc.2018.04.003.

[19] Mirghaderi R, Ahlehagh S. Effect of reduced brace section on behavior of SCBF bracings. AIP Conf. Proc, vol. 1020. American Institute of Physics; 2008. p. 1044–51.

[20] Ebrahimi S, Mirghaderi SR. A new friction–slip brace damper to improve seismic performance of braced frames. J Constr Steel Res 2023;207:107945. https://doi.org/10.1016/j.jcsr.2023.107945.

[21] Milani AS, Dicleli M. Comparative seismic behavior assessment of a new damper-equipped and conventional chevron-braced frames. J Constr Steel Res 2023;201:107720. https://doi.org/10.1016/j.jcsr.2022.107720.

[22] M. Rezai Prion HGL R. Tremblay N. Bouatay P. Timler. Seismic performance of brace fuse elements for concentrically braced steel frames. Behav. Steel Struct. Seism. Areas Proc Third Int Conf STESSA 2000 2000 21 24.

[23] Bonetti S. Ductile fuses for special concentrically braced frames. University of Kansas, 2008.

[24] Legeron F, Desjardins E, Ahmed E. Fuse performance on bracing of concentrically steel braced frames under cyclic loading. J Constr Steel Res 2014;95:242–55. https://doi.org/10.1016/j.jcsr.2013.12.010.

[25] Bazzaz M, Kafi MA, Kheyroddin A, Andalib Z, Esmaeili H. Evaluating the seismic performance of off-centre bracing system with circular element in optimum place. Int J Steel Struct 2014;14:293–304. https://doi.org/10.1007/s13296-014-2009-x.

[26] Andalib Z, Kafi MA, Kheyroddin A, Bazzaz M. Experimental investigation of the ductility and performance of steel rings constructed from plates. J Constr Steel Res 2014;103:77–88. https://doi.org/10.1016/j.jcsr.2014.07.016.

[27] Bazzaz M, Andalib Z, Kheyroddin A, Kafi MA. Numerical comparison of the seismic performance of steel rings in off-centre bracing system and diagonal bracing system. Steel Compos Struct 2015;19:917–37. https://doi.org/10.12989/scs.2015.19.4.917.

[28] Bazzaz M, Andalib Z, Kafi MA, Kheyroddin A. Evaluating the performance of OBS-C-O in steel frames under monotonic load. Earthq Struct 2015;8:699–712. https://doi.org/10.12989/eas.2015.8.3.699.

[29] Trombetti T, Silvestri S, Gasparini G, Ricci I. Stiffness-strength-ductility-design approaches for crescent shaped braces. Open Constr Build Technol J 2009;3:127–40. https://doi.org/10.2174/1874836800903020127.

[30] Mokhtari E, Laghi V, Palermo M, Silvestri S. Quasi-static cyclic tests on a half-scaled two-storey steel frame equipped with Crescent Shaped Braces. Eng Struct 2021;232:111836. https://doi.org/10.1016/j.engstruct.2020.111836.

[31] Palermo M, Laghi V, Gasparini G, Silvestri S, Trombetti T. Analytical estimation of the key performance points of the tensile force-displacement response of Crescent Shaped Braces. Soil Dyn Earthq Eng 2021;148:106839. https://doi.org/10.1016/j.soildyn.2021.106839.

[32] Palermo M, Pieraccini L, Dib A, Silvestri S, Trombetti T. Experimental tests on Crescent Shaped Braces hysteretic devices. Eng Struct 2017;144:185–200. https://doi.org/10.1016/j.engstruct.2017.04.034.

[33] Palermo M, Silvestri S, Gasparini G, Trombetti T. Crescent shaped braces for the seismic design of building structures. Mater Struct Constr 2015;48:1485–502. https://doi.org/10.1617/s11527-014-0249-z.

[34] Kammouh O, Silvestri S, Palermo M, Cimellaro GP. Performance-based seismic design of multistory frame structures equipped with crescent-shaped brace. Struct Control Heal Monit 2018;25:e2079. https://doi.org/10.1002/stc.2079.

[35] Boostani M, Rezaifar O, Gholhaki M. Introduction and seismic performance investigation of the proposed lateral bracing system called "OGrid. Arch Civ Mech Eng 2018;18:1024–41. https://doi.org/10.1016/j.acme.2018.02.003.

[36] Boostani M, Rezaifar O, Gholhaki M. Seismic performance investigation of new lateral bracing system called "OGrid-H. SN Appl Sci 2019;1:1–24. https://doi.org/10.1007/s42452-019-0369-8.

[37] Jouneghani HG, Haghollahi A, Moghaddam H, Moghadam AS. Study of the seismic performance of steel frames in the elliptic bracing. J Vibroengineering 2016;18:2974–85. https://doi.org/10.21595/jve.2016.16858.

[38] Ghasemi Jouneghani H, Haghollahi A, Moghaddam H, Sarveghad Moghadam A. Assessing seismic performance of the elliptic braced moment resisting frame through pushover method. J Rehabil Civ Eng 2019;7:68–85. https://doi.org/10.22075/JRCE.2018.13030.1232.

[39] Jouneghani HG, Haghollahi A. Experimental and analytical study in determining the seismic performance of the ELBRF-E and ELBRF-B braced frames. Steel Compos Struct 2020;37:571–87. https://doi.org/10.12989/scs.2020.37.5.571.

[40] Jouneghani HG, Fanaie N, Haghollahi A. Theoretical formulation for calculating elastic lateral stiffness in a simple steel frame equipped with elliptic brace. Struct Eng Mech 2022;45:437–54. https://doi.org/10.12989/scs.2022.45.3.437.

[41] Jouneghani HG, Fanaie N, Kalaleh MT, Mortazavi M. Determining elastic lateral stiffness of steel moment frame equipped with elliptic brace. Steel Compos Struct 2023;46:293–318. https://doi.org/10.12989/scs.2023.46.3.293.

[42] Jouneghani HG, Haghollahi A, Beheshti-Aval SB. Experimental study of failure mechanisms in elliptic-braced steel frame. Steel Compos Struct 2020;37:175–91. https://doi.org/10.12989/scs.2020.37.2.175.

[43] Jouneghani HG, Haghollahi A. Assessing the seismic behavior of steel moment frames equipped by elliptical brace through incremental dynamic analysis (IDA). Earthq Eng Eng Vib 2020;19:435–49. https://doi.org/10.1007/s11803-020-0572-z.

[44] Jouneghani HG, Haghollahi A, Kalaleh MT, Beheshti-Aval SB. Nonlinear seismic behavior of elliptic-braced moment resisting frame using equivalent braced frame. Steel Compos Struct 2021;40:45–64. https://doi.org/10.12989/scs.2021.40.1.045.

[45] Shamivand A, Akbari J. Ring-shaped lateral bracing system for steel structures. Int J Steel Struct 2020;20:493–503. https://doi.org/10.1007/s13296-019-00299-z.

[46] Fanaie N, Shirpour A. Analytical and numerical evaluation of quarter-elliptic-braced steel moment frames (QEB-MFs. Structures 2023;49:426–42. https://doi.org/10.1016/j.istruc.2023.01.100.

[47] Shirpour A, Fanaie N, Barzegar Seraji M. Seismic performance factors of quarter-elliptic-braced steel moment frames (QEB-MFs) using FEMA P695 methodology. Soil Dyn Earthq Eng 2024;178:108453. https://doi.org/10.1016/j.soildyn.2024.108453.

[48] Fanaie N, Shirpour A. Quasi-X-braced steel moment frames (QXB-MFs) evaluation using analytical and numerical methods. Bull Earthq Eng 2023:1–36. https://doi.org/10.1007/s10518-023-01778-9.

[49] Shirpour A, Fanaie N. Determining the seismic performance factors of quasi-X bracing systems. J Constr Steel Res 2024;212:108248. https://doi.org/10.1016/j.jcsr.2023.108248.

[50] Lee K, Foutch DA. Seismic evaluation of steel moment frame buildings designed using different R-values. J Struct Eng 2006;132:1461–72. https://doi.org/10.1061/(ASCE)0733-9445(2006)132:9(1461).

[51] Uang C-M. Establishing R (or Rw) and Cd factors for building seismic provisions. J Struct Eng 1991;117:19–28. https://doi.org/10.1061/(ASCE)0733-9445(1991)117:1(19).
[52] ATC-3–06. Tentative provisions for the development of seismic regulations for buildings 1978.
[53] ATC-19. Structural response modification factors 1995.
[54] ATC-34. A critical review of current approaches to earthquake-resistant design 1995.
[55] Maheri MR, Akbari R. Seismic behaviour factor, R, for steel X-braced and knee-braced RC buildings. Eng Struct 2003;25:1505–13. https://doi.org/10.1016/S0141-0296(03)00117-2.
[56] Kim J, Choi H. Response modification factors of chevron-braced frames. Eng Struct 2005;27:285–300. https://doi.org/10.1016/j.engstruct.2004.10.009.
[57] Mahmoudi M, Zaree M. Evaluating response modification factors of concentrically braced steel frames. J Constr Steel Res 2010;66:1196–204. https://doi.org/10.1016/j.jcsr.2010.04.004.
[58] Mwafy AM, Elnashai AS. Calibration of force reduction factors of RC buildings. J Earthq Eng 2002;6:239–73.
[59] Fanaie N, Ezzatshoar S. Studying the seismic behavior of gate braced frames by incremental dynamic analysis (IDA). J Constr Steel Res 2014;99:111–20. https://doi.org/10.1016/j.jcsr.2014.04.008.
[60] FEMA P695. Quantification of building seismic performance factors 2009.
[61] Farahi M, Mofid M. On the quantification of seismic performance factors of Chevron Knee Bracings, in steel structures. Eng Struct 2013;46:155–64. https://doi.org/10.1016/j.engstruct.2012.06.026.
[62] Asghari A, Saharkhizan S. Seismic design and performance evaluation of steel frames with knee-element connections. J Constr Steel Res 2019;154:161–76. https://doi.org/10.1016/j.jcsr.2018.11.011.
[63] Ghasemi M, Fanaie N, Khorshidi H. Seismic performance factors of a dual system with IMRF and cable-cylinder bracing. J Build Eng 2021;39:102309. https://doi.org/10.1016/j.jobe.2021.102309.
[64] Shahiditabar A, Moharrami H, Snijder HH. Quantification of seismic performance factors of self-centered y-shaped braced frames. J Constr Steel Res 2022;194:107304. https://doi.org/10.1016/j.jcsr.2022.107304.
[65] Bakhshivand E, Ahmadie Amiri H, Maleki S. Evaluation of seismic performance factors for dual steel SMF-SCBF systems using FEMA P695 methodology. Soil Dyn Earthq Eng 2022;163:107506. https://doi.org/10.1016/j.soildyn.2022.107506.
[66] Mahmoudi M, Mehrizi AZ, Shirpour A. Evaluation of the effect of end-connection specifications on lateral bearing capacity of concentrically braced steel frames. Int J Steel Struct 2018;18:179–87. https://doi.org/10.1007/s13296-018-0314-5.
[67] Simulia DS. Abaqus 6.14 user's manual. Providence, RI: Dassault Systems; 2014.
[68] Mahmoudi M, Shirpour A, Zarezadeh A. The effects of mid-span connection specifications on compressive performance of cross (X) braces. Int J Steel Struct 2019;19:1125–33. https://doi.org/10.1007/s13296-018-0192-x.
[69] EN 1993–1-1. Eurocode 3: Design of steel structures - Part 1–1: General rules and rules for buildings. vol. 1. European Committee for Standardisation, Brussels; 2005.
[70] Lee J, Lee C, Kim B. Reverse analysis of nano-indentation using different representative strains and residual indentation profiles. Mater Des 2009;30:3395–404. https://doi.org/10.1016/j.matdes.2009.03.030.
[71] ATC-24. Guidelines for cyclic seismic testing of components of steel structures 1992.
[72] Jouneghani HG, Haghollahi A. Experimental study on hysteretic behavior of steel moment frame equipped with elliptical brace. Steel Compos Struct 2020;34:891–907. https://doi.org/10.12989/scs.2020.34.6.891.
[73] ASCE/SEI 7–22. Minimum Design Loads and Associated Criteria for Buildings and Other Structures 2022.
[74] ANSI/AISC 360–16. Specification for structural steel buildings 2016.
[75] ANSI/AISC 341–16. Seismic provisions for structural steel buildings 2016.
[76] Mazzoni S, McKenna F, Scott MH, Fenves GL. OpenSees command language manual. Pac Earthq Eng Res Cent 2006;264:137–58.
[77] Karamanci E, Lignos DG. Computational approach for collapse assessment of concentrically braced frames in seismic regions. J Struct Eng 2014;140. https://doi.org/10.1061/(asce)st.1943-541x.0001011.
[78] Lignos DG, Asce M, Hartloper AR, Asce SM, Elkady A, Asce AM, et al. Proposed updates to the ASCE 41 nonlinear modeling parameters for wide-flange steel columns in support of performance-based seismic engineering 2019;145:1–13. https://doi.org/10.1061/(ASCE)ST.1943-541X.0002353.
[79] Lignos DG, Krawinkler H. Deterioration modeling of steel components in support of collapse prediction of steel moment frames under earthquake loading. J Struct Eng 2011;137:1291.
[80] Lignos DG, Krawinkler H. A steel database for component deterioration of tubular hollow square steel columns under varying axial load for collapse assessment of steel structures under earthquakes. Proc 7th Int Conf Urban Earthq Eng 2010.
[81] NIST 2017b. Guidelines for Nonlinear Structural Analysis for Design of Buildings Part IIa–Steel Moment Frames 2017. https://doi.org/10.6028/NIST.GCR.17–917-46v2.
[82] Gupta A. Seismic demands for performance evaluation of steel moment resisting frame structures. Stanford University; 1999.
[83] ASCE/SEI 41–06. Seismic Rehabilitation of Existing Buildings 2006. https://doi.org/10.1126/science.1.3.84.
[84] Vamvatsikos D, Cornell CA. Incremental dynamic analysis. Earthq Eng Struct Dyn 2002;31:491–514. https://doi.org/10.1002/eqe.141.
[85] Baker JW, Cornell CA. Spectral shape, epsilon and record selection. Earthq Eng Struct Dyn 2006;35:1077–95. https://doi.org/10.1002/eqe.571.
[86] Haselton CB, Baker JW, Liel AB, Deierlein GG. Accounting for ground-motion spectral shape characteristics in structural collapse assessment through an adjustment for epsilon. J Struct Eng 2011;137:332–44. https://doi.org/10.1061/(asce)st.1943-541x.0000103.